NASA TECHNICAL REPORT

NASA TR R-308

A SEARCH FOR GAMMA-RAYS FROM THE CRAB NEBULA USING A DIGITIZED SPARK CHAMBER

by Donald Avery Kniffen

Goddard Space Flight Center
Greenbelt, Md.

NATIONAL AERONAUTICS AND SPACE ADMINISTRATION • WASHINGTON, D. C. • MAY 1969

NASA TR R-308

A SEARCH FOR GAMMA-RAYS FROM THE CRAB NEBULA USING A DIGITIZED SPARK CHAMBER

By Donald Avery Kniffen

Goddard Space Flight Center
Greenbelt, Md.

NATIONAL AERONAUTICS AND SPACE ADMINISTRATION

For sale by the Clearinghouse for Federal Scientific and Technical Information
Springfield, Virginia 22151 – CFSTI price $3.00

ABSTRACT

Gamma-ray astronomy provides an opportunity to obtain information directly related to the physical processes taking place within celestial objects; processes that may also give rise to the energetic charged particle cosmic-rays. The detection of celestial gamma-ray point sources may shed some light on the origin of cosmic-rays.

The study of high-energy photons is necessarily a very new field of astrophysics, because the short path length of the quanta in air makes it necessary to place the observing instruments above the atmosphere. No γ-ray point source has been detected for certain; however, several significant upper limits to possible sources have been obtained. One of the most likely sources, the Crab nebula, was chosen for investigation in this experiment.

The detector developed for this investigation is a digitized spark chamber, mounted in an oriented gondola and flown by balloon above all but a small amount of the earth's atmosphere. The detector is triggered by a scintillation-counter Čerenkov-detector charged-particle telescope, in the event that no charged particle has passed through the anticoincidence scintillator that surrounds the entire detector.

Analysis of the data consists of examining each event recorded during the flight for the pair-production events. The celestial arrival direction of each gamma-ray is estimated by the bisector of the pair. The construction of the chamber with many thin plates alternated with the spark modules allows a determination of the gamma-ray energy in the 30- to 250-Mev energy range by the multiple scattering technique.

Though no celestial source of gamma-rays was detected, upper limits of 2.3 and 1.8×10^{-4} cm^{-2} sec were obtained for photons from the Crab nebula with energies $30 \leq E_\gamma \leq 100$ and $E_\gamma > 100$ Mev, respectively. The differential and integral energy spectra of gamma-rays produced in the atmosphere at a depth of 3 g/cm^2 were obtained in the 30-250 Mev energy range.

CONTENTS

A SEARCH FOR GAMMA-RAYS FROM THE CRAB NEBULA USING A DIGITIZED SPARK CHAMBER*

by
Donald Avery Kniffen
Goddard Space Flight Center

CHAPTER I

INTRODUCTION

Until recent years, ground-based observations in optical and radio astronomy provided the bulk of available astrophysical data, but these observations give only very indirect information relative to the thermonuclear processes of energy release. Without an observable neutrino signal of cosmic origin, it is impossible to obtain direct information on such processes. In 1958 Morrison suggested another class of energy-releasing processes, important to stellar evolution, that might be accessible to direct observation via primary cosmic-rays and energetic gamma-rays (Morrison, 1958). Because of the well-known isotropic nature of primary cosmic-ray charged particles resulting from the interaction of the charged particles with the interstellar magnetic fields, observed processes cannot be identified with a particular source region. Therefore, the study of energetic cosmic gamma-rays—the detection of their sources and measurement of their spectra—offers the best clue to the nuclear processes that take place within celestial objects and possibly give rise to the energetic charged particle cosmic-rays.

In addition to point sources, there is undoubtedly a diffuse background of gamma-rays, as has already been established for X-ray energies (Oda, 1965, p. 68, and Rossi, 1966, p. 383). The measurement of such diffuse intensities (which would arise from mechanisms similar to those for point sources) should provide important information about conditions in interstellar space.

Only recently has it become feasible to study energetic cosmic photons, since the interaction length for high-energy electromagnetic interactions is approximately a radiation length 40 g/cm^{-2} of air, corresponding to a height above sea level of about 80,000 feet. This makes it necessary to make these photon observations from balloons or satellites, to avoid masking the events to be studied by the interaction of primary gamma-rays within the atmosphere and (more important) by secondary gamma-ray production by nuclear interactions of charged cosmic-ray particle primaries within the atmosphere.

*Submitted to the faculty of the Graduate School of Arts and Sciences Of The Catholic University of America in partial fulfillment of the requirements for the degree Doctor of Philosophy, 1967.

From known but rather uncertain parameters for conditions within the possible source regions, we can predict the flux of gamma-rays to be expected at the earth's surface, from the various theoretically possible production mechanisms. For most mechanisms in the gamma-ray energy range above 30 Mev chosen for this experiment, the Crab nebula (Taurus A—a remnant of supernova 1054 A.D.) appears to be one of the likeliest sources to yield an observable flux; this source was chosen for observation. High-energy (≥20 kev) X-rays, recently observed in the direction of the Taurus A region (Peterson *et al.*, 1966), promise a view of the more energetic gamma-rays. Predictions of the probable fluxes will be discussed in the next chapter.

Many experiments, using a variety of detection techniques, have been performed to search for gamma-rays with energies greater than 30 Mev from several possible discrete sources (see Perlow and Kissinger, 1951; Bracessi *et al.*, 1960; Danielson, 1960; Cline, 1961; Klarmann, 1962; Kraushaar and Clark, 1962a and 1962b; Cobb *et al.*, 1965; Fichtel and Kniffen, 1965; Kraushaar *et al.*, 1965; Duthie *et al.*, 1966; Frye *et al.*, 1966, Frye and Smith, 1966; Frye and Wang, 1967; Fazio and Hafner, 1967; Fazio, *et al.*, 1967; Fazio and Helmken, 1968; Delvaille, *et al.*, 1968; Frye and Wang, 1968; and Fichtel, *et al.*, 1968), but no unambiguous positive results have been obtained. In recent years the search has continued with detectors of increasing sensitivity, but ultimately it will be necessary to perform the experiments on satellites. The background of secondary gamma-rays produced in the atmosphere in nuclear interactions induced by energetic charged particle cosmic-rays sets a rather stringent limit of about 10^{-5} photons cm^{-2} sec^{-1} on the observable point-source flux limit for photons with energies greater than 30 Mev in balloon experiments, and makes a measurement of the diffuse intensity extremely difficult if not impossible. No attempt was made in this experiment to measure the diffuse intensity. Many types of detectors have been used in gamma-ray astronomy; Greisen (1966) has made a comprehensive review of the techniques and problems encountered. The detector used in this experiment herein described is a digitized wire-grid spark chamber that is placed in an oriented gondola and suspended from high-altitude research balloons. Chapter III discusses the many advantages of this type of spark chamber for gamma-ray studies in space.

CHAPTER II

GAMMA-RAY PRODUCTION MECHANISMS

1. Introduction

This chapter discusses the various production mechanisms by which gamma-rays with energies greater than 30 Mev might be produced in source regions. On the basis of known physical parameters in the Crab nebula (Taurus A), estimates can be made of the flux levels from such a source that might be observed on the earth. The possibility of observing the predicted flux levels will then be discussed.

The mechanisms that may produce gamma-rays above 30 Mev (7×10^{21} Hz) are well-known nuclear and electromagnetic processes and have been reviewed by various authors in the context of gamma-ray astronomy (see Morrison, 1958; Savedoff, 1959; Dolan and Fazio, 1965; Hayakawa, *et al.*, 1964; Garmire and Kraushaar, 1965; Ginzburg and Syrovatskii, 1965) Gould and Burbidge, 1965; and Fazio, 1967). The most important processes expected to occur within the Crab when emitting gamma-rays at these high energies, appear to be: the decay of π^0-mesons produced by nuclear collisions within the source, bremsstrahlung radiation emitted by electrons traversing the matter within the source, Compton radiation resulting from the collision of energetic electrons with low-energy photons, and synchrotron radiation emitted by energetic electrons spiraling in magnetic fields within the source region. The best estimate of the flux of gamma-rays that might reach the earth will be considered in the following sections for each of these mechanisms.

2. 30-Mev Gamma-Rays from Synchrotron Radiation

Observations of electromagnetic radiation from the Crab nebula have been made in the optical, radio, and X-ray energy regions; both the radio and optical spectral fluxes can be adequately accounted for by synchrotron emission from energetic electrons traveling under the influence of magnetic fields within the source region. This explanation is supported by the strong polarization observed in the optical continuum emitted by the Crab, and to a lesser extent in the radio emission where polarization measurements are more difficult. However, unless energetic electrons are produced or accelerated locally in great abundance, this is not a likely source of X-rays, much less γ-rays.

The energy radiated by an electron moving in an orbit of radius $r_L = E_e/eH_\perp$ is given by

$$\left(\frac{dE_e}{dt}\right)_{sync} = \frac{2}{3}\frac{e^4 H_\perp^2}{m_e^2 c^3}\left(\frac{E_e}{m_e c^2}\right)^2 , \qquad (2.1)$$

with a larmor frequency $\nu_L = eH/2\pi m_e c$. The energy spectrum peaks at a frequency

$$\nu_{max} \approx 0.44\,\nu_L \left(\frac{E_e}{m_e c^2}\right)^2 \tag{2.2}$$

$$\approx 1.26 \times 10^6\, H_\perp \left(\frac{E_e}{m_e c^2}\right)^2 . \tag{2.2'}$$

(See Ginzburg and Syrovatskii, 1964, pp. 366 and 367.)

Assuming a source intensity of electrons

$$n_e\left(E_e\right) dE_e = K_e\, E_e^{-\Gamma_e}\, dE_e \ \text{cm}^{-3} , \tag{2.3}$$

we can calculate the energy flux of synchrotron emission observed at the earth:

$$F(\nu) = \frac{1}{4\pi} \int\limits_{\substack{\text{source} \\ \text{vol.}}} \int\int\int_{E_e = h\nu}^{\infty} n_e\left(E_e\right) P\left(\nu, E_e\right) dE_e\, dr\, d\Omega \ \text{ergs cm}^{-2}\ \text{sec}^{-1}\ \text{Hz}^{-1} , \tag{2.4}$$

where $P\left(\nu, E_e\right)$ is the energy radiated per second by an electron of energy E_e in a frequency interval $d\nu$ centered about ν. We may approximate $P\left(\nu, E_e\right)$ by

$$P\left(\nu, E_e\right) = \left(\frac{dE_e}{dt}\right)_{sync} \delta\left[\nu - 0.44\,\nu_L \left(\frac{E_e}{m_e c^2}\right)^2\right] . \tag{2.5}$$

Inserting Equations 2.1, 2.2, 2.3, and 2.5 in Equation 2.4, we obtain

$$F_{\gamma,sync}\ (\nu) = \frac{1}{4\pi s^2} \int\limits_{\substack{\text{source} \\ \text{vol.}}} \int\int\int_{E_e = h\nu}^{\infty} K_e\, E_e^{-\Gamma_e} \left[\frac{2}{3} \frac{e^4 H}{m_e c^3} \left(\frac{E_e}{m_e c^2}\right)^2\right] \delta\left[\nu - 0.44\,\nu_L \left(\frac{E_e}{m_e c^2}\right)^2\right] dE_e\, dV_0$$

$$= 1.98 \times 10^{-23}\, \frac{K_e V_0 H^{\left(\Gamma_e + 1\right)/2}}{s^2} \left(\frac{6.26 \times 10^{18}}{\nu}\right)^{\left(\Gamma_e - 1\right)/2} \ \text{ergs cm}^{-2}\ \text{sec}^{-1}\ \text{Hz}^{-1} , \tag{2.6}$$

where V_0 is the source volume and $H_\perp^2 \approx (2/3)H^2$. The essential feature of this result is that observation of a spectral flux at the earth of the form $F_\nu = C\nu^{-\alpha_\nu}$ implies an electron source spectrum of the form

$$n_e = K_e\, E_e^{-(1+2\alpha_\nu)} . \tag{2.7}$$

Consequently, if it can be assumed that such a spectrum continues to higher frequencies, an extrapolation over several decades of energy will provide an expected X-ray and γ-ray flux. However, the probable lifetimes of the source electrons indicate that such an extrapolation may not be justified.

If field strength = 3×10^{-4} gauss, (Shklovskii, 1960, p. 339), Equation 2.1 gives

$$\left(\frac{dE_e}{dt}\right)_{sync} \Big/ E_e = 8.82 \times 10^{-17} \frac{E_e}{(m_e c^2)^2}$$

$$= \left(3.37 \times 10^{-16} E_e\right)/\text{sec}$$

$$= \frac{1}{\tau_{sync}} \cdot \qquad (2.8)$$

For a given frequency of emission, Equation 2.2' gives

$$E_e = 0.0262 \sqrt{\nu} \text{ Mev} , \qquad (2.9)$$

which may then be inserted in Equation 2.8 to give τ_{sync}. Table 2.1 summarizes the results over the major frequency ranges of observed fluxes. Table 2.1 shows that, under the assumptions made, radio and possibly optical emission (within the errors of the estimates) may be due to emission by

Table 2.1

Lifetime of Crab Nebula Electrons Against Synchrotron Emission.

Category	Radio	Optical	X-ray
Frequency (Hz)	1×10^9	6×10^{14}	6×10^{17}
sync (sec)	3.6×10^{12}	4.6×10^9	1.4×10^8

energetic electrons produced at the time of the supernova (913 years or about 3×10^{10} seconds ago). However, X-ray emission would have depleted the supply of 2×10^{13} Mev electrons; local production and/or acceleration of electrons within the source region would be necessary to have maintained X-ray emission since the year 1054. Figure 2.1, depicting the break in the power-law component of the observed spectral emission just below the optical

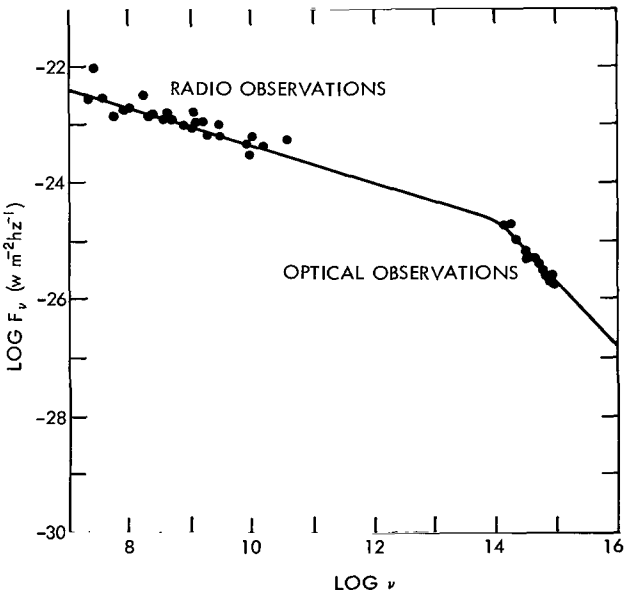

Figure 2.1—Plot of the log of the observed differential intensity vs the log of the frequency. This graph is taken from the work of Gould and Burbidge (1965).

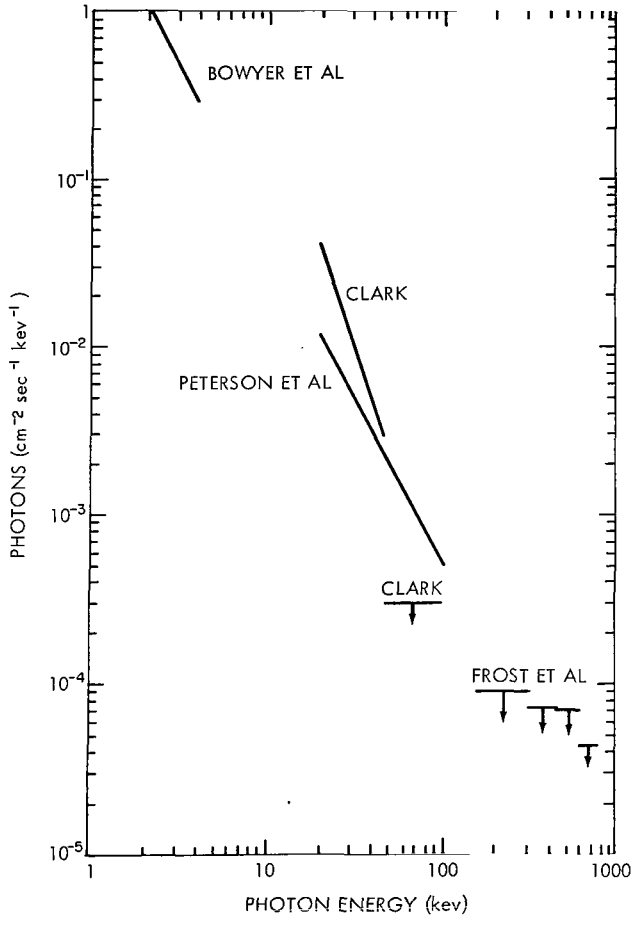

Figure 2.2—The measured Crab nebula differential X-ray spectra and upper limits from the work of Peterson, et al. (1966), Bowyer, et al. (1964), Clark (1965), and Frost, et al. (1966).

frequency, gives support to the numbers and assumptions used to obtain Table 2.1, assuming that the electrons giving rise to the lower-energy photons were generated at the time of the supernova. Possibly, then, the break in the spectrum at about 10^{14} Hz (which implies a break in the electron spectrum at about 2.6×10^{11} ev) indicates the point at which energy losses have severely depleted the primary electrons and second-generation electrons become important. Since $\alpha_\nu = 0.28$ below 10^{14} Hz and about 1.09 above this frequency, this implies a change in the slope Γ_e of the electron spectrum from 1.56 to 3.18.

It is, of course, impossible to predict the electron spectrum at higher energies; hence, the most reasonable procedure is to extrapolate the observed photon spectrum to higher frequencies or energies over the shortest possible energy interval. To do this we use the Crab X-ray measurements of Peterson, *et al.* (1966) in the 16- to 120-kev range. His results, shown in Figure 2.2 along with other Crab X-ray observations, may be expressed as $dN_\gamma/dE_\gamma = 3.7 E_\gamma^{-1.91} \pm 0.08$, which extrapolated to higher energies yields a predicted flux of photons, with energies greater than 30 Mev, of 4.4×10^{-4} cm^{-2} sec^{-1}. The observed slope indicates a further steepening of the photon spectrum at the higher energies. The extrapolated flux requires a source of electrons with energies greater than 3×10^{14} ev (assuming a 3×10^{-4} gauss field). It is unlikely that electrons are available within the source at these energies at a sufficient intensity to explain the observations by synchrotron emission.

3. 30-Mev Gamma-Rays from Bremsstrahlung

To estimate the special flux of photons emitted by the bremsstrahlung radiation of relativistic electrons as they penetrate the matter in the source region, we will use the approximate expression for the effective differential cross section (Fermi, 1955, p. 47) $\sigma_{rad}(E_e, E_\gamma)\, dE_\gamma \sim (nm/X)\, dE_\gamma/E_\gamma$, where m is the mass of the atoms in the gas, n is their density, and X is the radiation length. Then the photon number flux to be expected at the earth is

$$F_{\gamma,br}(E_\gamma) = \frac{c}{4\pi s^2} \int_{E_\gamma}^{\infty} \iiint_{\substack{\text{source} \\ \text{vol.}}} K_e E_e^{-\Gamma_e} \frac{nm}{E_\gamma X}\, dE_e\, dV_0 \qquad (2.10)$$

is the spectral flux of emitted photons. Thus

$$F_{\gamma,br}(E_\gamma) = \frac{cK_e M E_\gamma^{-\Gamma_e}}{4\pi s^2 X(\Gamma_e - 1)}, \tag{2.11}$$

where M denotes the total mass within the source. The cross section and Equation 2.10 show that we are concerned with electrons with energies in the region $\gtrsim$30 Mev, which by Equation 2.2' emits photons of 10^6 Hz and above. This is in the region of radio emission; hence, by using Equation 2.6 and the observed intensity of radio emission, we may obtain K_e. Using a radio emission flux density of 1.7×10^{-23} w m^{-2} Hz^{-1} at 10^8 Hz (Ginzburg and Syrovatskii, 1964, p. 112), a source distance of 1.1 kpc, a field of 3×10^{-4} gauss, and with $\Gamma_e = 1.56$, we obtain $K_e = 9.45 \times 10^{-9}$ cm^{-3} ev^{-1}. Inserting this value in Equation 2.11, with M equal to 2×10^{32} grams (Ginzburg and Syrovatskii, 1965) and with X equal to 52 grams cm^{-2} (Garmire and Kraushaar, 1965), the observed integral gamma-ray spectrum at the earth should be 8.4×10^{-8} $E_\gamma^{-0.56}$ photons cm^{-2} sec^{-1} for E_γ in Mev. This yields a flux greater than 30 Mev of 1.3×10^{-8} photons cm^{-2} sec^{-1}, well below the sensitivity of existing detectors and measurements.

Sartori and Morrison (1967) have presented an argument in favor of the thermal bremsstrahlung mechanism from a dilute and very hot plasma in the remnant supernova shell, to explain the observed Crab X-ray intensities; the mechanism is not considered here, since unreasonably hot plasmas would be required to produce photons in the hard gamma-ray energy region.

4. 30-Mev Gamma-Rays from Compton-Scattering

The importance of the collision of cosmic-ray electrons with thermal photons in galactic space was first pointed out by Feenberg and Primakoff (1948). More recently Felten and Morrison (1963) have considered this mechanism as a possible source of galactic X-rays and gamma-rays. The process can also be applied to point sources such as the Crab nebula.

The well known Compton-scattering formula for the interactions of an energetic photon with an electron which is initially at rest is

$$\epsilon_r' = \frac{\epsilon_r}{1 + (\epsilon_r / m_e c^2)(1 - \cos\chi_r)} \tag{2.12}$$

in the rest frame of the target electron where χ_r is the photon scattering angle. In the earth's frame

$$\epsilon_r = \gamma_e \epsilon_\ell (1 - \beta_e \cos\theta), \tag{2.13}$$

where β_e is the velocity of the electron, $\gamma_e = E_e / m_e c^2$, and $\pi - \theta$ is the angle between the direction of the primary electron and the direction of the photon before scattering.

Also, of course,

$$\epsilon_r' = \gamma_e \epsilon_\ell' \left(1 - \beta_e \cos\theta'\right) , \tag{2.13'}$$

where $\pi - \theta'$ is the angle between the direction of the scattered electron and photon. For isotropic photon emission, and electron distribution,

$$\overline{\epsilon_r'} = \overline{\gamma_e \epsilon_\ell'} \quad \text{and} \quad \overline{\epsilon_r} = \overline{\gamma_e \epsilon_\ell} .$$

For $\gamma_e \left(\epsilon_\ell / m_e c^2\right) \ll 1$, the Thomson cross section is applicable (Heitler, 1954, p. 35) and the differential cross section is given by

$$d\sigma_T = \frac{1}{2} r_e^2 \left(1 + \cos^2 \chi_r\right) d\Omega . \tag{2.14}$$

The total cross section is therefore

$$\sigma_T = \int d\sigma_T = \frac{8\pi}{3} r_e^2 = \frac{8\pi}{3} \left(\frac{e^2}{m_e c^2}\right)^2 = 6.65 \times 10^{-25} \text{ cm}^2 ,$$

where $\Omega = 2\pi \sin\chi_r \, d\chi_r$ for $\overline{\epsilon_r} = \overline{\gamma_e \epsilon_\ell} \ll m_e c^2$, Equation 2.12 averaged over isotropic space gives

$$\overline{\epsilon_r'} \approx \overline{\epsilon_r} - \frac{\overline{\epsilon_r^2}}{m_e c^2} ,$$

and the electron energy subsequent to scattering in the rest frame of the primary electron is

$$\overline{E_r'} = \overline{\epsilon_r} - \overline{\epsilon_r'} = \frac{\overline{\epsilon_r^2}}{m_e c^2} \tag{2.15}$$

The longitudinal momentum of the electron is given (Ginzburg and Syrovatskii, 1964, p. 144) by

$$\overline{P_r'} = \int \frac{\overline{\epsilon_r}}{c} \left(1 - \cos\theta\right) \frac{d\sigma_T}{\sigma_T} = \frac{\overline{\epsilon_r}}{c} ; \tag{2.15'}$$

hence, the transformation to the laboratory frame yields for the mean energy transferred to a thermal photon:

$$\overline{\Delta\epsilon_\ell} = -\gamma_e\left(\overline{E_r'} + c\beta_e\,\overline{P_r'}\right)$$

$$\approx -\gamma_e\, c\overline{P_r'} = -\frac{\overline{\epsilon_r}\,E_e}{m_e c^2} \quad \left(\text{if } \beta_e = 1, \text{ and } \epsilon_r \ll m_e c^2\right)$$

$$= -\overline{\epsilon_\ell}\left(\frac{E_e}{m_e c^2}\right)^2 . \tag{2.16}$$

Recall that $\overline{\epsilon}_\ell$ and E_e are the photon and electron energies prior to scattering, in the laboratory frame. Finally, then, for this case

$$-\left(\frac{dE_e}{dt}\right)_{comp} = c\sigma_T\,\overline{n}_{ph}\,\overline{\Delta\epsilon_\gamma'} = c\sigma_T\,\rho_{ph}\,\gamma_e^2$$

$$= 2.7\times 10^{-20}\,\rho_{ph}\,\gamma_e^2 \text{ Mev sec}^{-1} , \tag{2.17}$$

where $\overline{n}_{ph}$ is the average photon number density and ρ_{ph} is the energy density of the photon field which scatters the electrons.

For the case where $\gamma_e\left(\overline{\epsilon_\ell}/m_e c^2\right) \ll 1$, we obtain (Feenberg and Primakoff, 1948) $-\overline{\Delta\epsilon_\ell} \approx E_e$, and the asymptotic form of the Klein-Nishina cross section

$$\sigma = \frac{3}{8}\,\sigma_T\left(\frac{m_e c^2}{\overline{\epsilon_r}}\right)\left(\ln\frac{2\epsilon_r}{m_e c^2} + \frac{1}{2}\right) \tag{2.18}$$

is applicable. The Compton energy losses by the electron are then

$$-\left(\frac{dE}{dt}\right)_{comp} \approx c\sigma\,\overline{n}_{ph}\,E_e . \tag{2.19}$$

To estimate the flux of photons expected from this process we use the procedure analogous to the case for synchrotron emission discussed in Section 2. This gives

$$F_{\gamma,comp}\left(E_\gamma\right) = \frac{V_0}{s^2}\,\rho_{ph}\left(1.8\times 10^{-14}\right)\left(2.5\times 10^{3}\right)^{\Gamma_e-1}\times\left(\overline{\epsilon}_\ell\right)^{\Gamma_e-3/2}K_e\,E_\gamma^{-(\Gamma_e+1)/2}$$

$$= 3.6\times 10^{-7}\,E_\gamma^{-(\Gamma_e+1)/2} . \tag{2.20}$$

where E_γ is in ev, ρ_{ph} the photon energy density in ev cm^{-3} is taken to be 1.7 (Garmire and Kraushaar, 1965), $\bar{\epsilon}_\ell$ is about 2 ev, and the remaining units and constants are the same as before. For $\Gamma_e = 1.56$ this yields an integral spectrum of $5.4 \times 10^{-8} E_\gamma^{-0.28}$ cm^{-2} sec^{-1}, where E_γ is the photon energy expressed in Mev. The resulting photon flux above 30 Mev at the earth would be 2.1×10^{-8} cm^{-2} sec^{-1}, again below presently detectable levels.

Equation 2.16 shows that Compton processes are more efficient when the average photon energy is higher, as in the hot plasma region suggested by Sartori and Morrison (1967) but the assumed Maxwellian distribution of electrons at a temperature of 40 kev is not enough to produce photons efficiently by the Compton process in the gamma-ray energy region, unless a much higher temperature plasma is invoked.

5. 30-Mev Gamma-Rays from Pion Decay

The production of pi-mesons in the high-energy nuclear interactions when energetic cosmic ray particles traverse matter is a well known and studied phenomenon. It is precisely this process occurring within the terrestrial atmosphere that led to the discovery of the pion. The process also occurs within such sources of relatively high-density matter as the Crab nebula, giving rise to both charged and neutral mesons. The uncharged mesons constitute roughly one-third of the pions that are produced and that decay by the process

$$\pi^0 \rightarrow \gamma + \gamma \ ,$$

where each of the gamma-rays carries off 67.5 Mev in the rest frame of the π^0 and an energy between $67.5 \sqrt{(1-\beta_\pi)/(1+\beta_\pi)}$ and $67.5 \sqrt{(1+\beta_\pi)/(1-\beta_\pi)}$ in the laboratory system; β_π is the velocity of the π^0.

The pions result primarily from nucleon-nucleon collisions; therefore, in order to estimate the pi-zero decay contribution to gamma-ray flux, we must know the energetic nucleon spectrum within the source region as well as the matter density. Unfortunately, there is no direct way to estimate the nucleon spectrum for the Crab nebula; an indirect method must be used which gives an upper bound to the expected flux at the earth. This approach necessitates assuming that the synchrotron electrons now observed have been continuously produced since the time of the supernova by nuclear interactions that also formed neutral pions. The observed radio emission may be used to estimate the electron spectrum and (through the particle kinematics) the pion spectrum.

The electrons arise through the decays

$$\pi^\pm \rightarrow \mu^\pm + \nu$$

and

$$\mu^\pm \rightarrow e^\pm + 2\nu \ .$$

In the pion decay the muon carries off only 4 of the available 30-Mev kinetic energy; hence we can make the approximation $E_\mu \approx (m_\mu/m_\pi)\, E_\pi$. In the muon decay, the electron rest mass is negligible compared to the available energy; hence, the electron and neutrinos behave alike kinematically, allowing the approximation

$$E_e \approx \frac{1}{3} E_\mu = \frac{1}{3}\left(\frac{m_\mu}{m_\pi}\right) E_\pi \ .$$

Thus, given a pion production spectrum $K_\pi E_\pi^{-\Gamma_\pi}\, dE_\pi/\tau$, we may obtain an electron production spectrum from

$$q_e(E_e)\, dE_e = \frac{K_e E_e^{-\Gamma_e}}{\tau}\, dE_e \approx \frac{2}{3}\int \frac{K_\pi E_\pi^{-\Gamma_\pi}}{\tau}\, f(E_e, E_\pi)\, dE_\pi\, dE_e \ ,$$

where the 2/3 factor occurs because of the requirement for charged pions. Function $f(E_e, E_\pi)$ may be approximated by

$$\delta\left[E_e - \frac{1}{3}\left(\frac{m_\mu}{m_\pi}\right)E_\pi\right] \approx \delta\left(E_e - \frac{E_\pi}{4}\right) \ ,$$

resulting in

$$K_e E_e^{-\Gamma_e}\, dE_e \approx \frac{8}{3} K_\pi (4)^{-\Gamma_e+1} E_e^{-\Gamma_e}\, dE_e \ . \tag{2.21}$$

Therefore K_e and K_π are related by

$$\frac{K_e}{K_\pi} = \frac{8}{3}(4)^{-(\Gamma_e-1)} \ . \tag{2.22}$$

If the pi-meson production spectrum is given by $q_\pi(E_\pi) = K_\pi E_\pi^{-\Gamma_\pi}/\tau$ with the neutral pions decaying into two photons, we may approximate the resulting photon spectrum by assuming that one-third of the pions are π^0's, which decay into two gamma-rays, each with energy $E_\pi/2$. This gives a photon production spectrum of

$$q_\gamma(E_\gamma) \approx \frac{1}{4}(2)^{\Gamma_e-1} K_e E_\gamma^{-\Gamma_e}/\tau \ , \tag{2.23}$$

where τ is the age of the nebula. These assumptions lead to a predicted differential flux at the earth of

$$F_{\gamma,\pi^0}(E_\gamma) = \frac{V_0}{4\pi s^2} q_\gamma(E_\gamma) = \frac{V_0 K_e (2)^{\Gamma_e-1}}{16\pi^2 s^2 \tau} E_\gamma^{-\Gamma_e} \ . \tag{2.24}$$

Using the same values for the parameters as before, this gives a differential flux at the earth of $1.9 \times 10^{-4}\ E_\gamma^{-1.56}\ cm^{-2}\ sec^{-1}\ Mev^{-1}$. The integral flux is thus $3.5 \times 10^{-4}\ E_\gamma^{-0.56}\ cm^{-2}\ sec^{-1}$ giving an integrated flux above 30 Mev of $5.2 \times 10^{-5}\ cm^{-2}\ sec^{-1}$. It must be stressed that this is an upper limit to the flux estimate from this process, since the lifetimes given in Section 2 indicate that there may be a major contribution to the electrons within the Crab nebula from electrons formed during the initial explosion.

6. Summary

To establish whether the flux estimates obtained in these considerations are detectable within the present state of technology, it is necessary to define a detectable flux. The minimum detectable point source flux may be approximated by using the formula given by Greisen (1966), where the limit is given by

$$F_{\gamma,min} = N_\sigma \left[\frac{I_{\gamma,b.g.}\ \Omega}{\alpha\ At\ f}\right]^{1/2}, \tag{2.25}$$

where $I_{\gamma,b.g.}$ is the diffuse background gamma-ray intensity, At is the area-time factor for the detector, α is the efficiency of the detector for gamma-ray detection, Ω is the solid-angular resolution of the detector system, f is that portion of t during which the detector is live, and N_σ is the signal-to-noise factor required to define a detectable flux. (Equation 2.25 assumes a nearly perfect anticoincidence system for discriminating against charged-particle cosmic-rays.) Letting N_σ equal 5 and using the values for the detector system discussed in Chapter III (and typical of those applying to present day balloon detectors) gives

$$F_{\gamma,min} = 1.6 \times 10^{-5}\ cm^{-2}\ sec^{-1}\ . \tag{2.26}$$

From the possible production mechanisms discussed, only the extrapolated observed power law spectrum and the π^0-decay contribution seem likely to provide a detectable flux as summarized in Table 2.2. Unfortunately, it is these mechanisms that are the most likely to be overestimated, possibly by a substantial amount. However, these flux estimates should not be taken too seriously, since the estimates of the electron spectrum, field strengths, source distance, photon energy density, and all other parameters required in the calculations are based on very indirect information and, if different assumptions were made concerning conditions in the source region, could greatly alter the estimates. Admittedly, the prospect of

Table 2.2

Predicted Gamma-Ray Fluxes from the Crab Nebula.

Mechanism	Predicted F ($E_\gamma > 30$ Mev) ($cm^{-2}\ sec^{-1}$)
Extrapolated X-ray spectrum	4.4×10^{-4}
Bremsstrahlung	1.3×10^{-8}
Compton scattering	2.1×10^{-8}
Neutral pion decay	5.2×10^{-5}

locating a detectable source is discouraging, with existing levels of detector sensitivity. Nevertheless, the search for a gamma-ray flux should go on, with such increasing sensitivity as the technology allows. This is because of the importance of astrophysical data that can be obtained only through this mode of radiation. Furthermore, the possibility always exists that unexpectedly intense flux levels might be encountered.

CHAPTER III

THE DETECTOR

1. Introduction

In the gamma-ray energy region chosen for examination, $E_\gamma \geq 30$ Mev, the dominant process lending itself to the detection and study of energetic photons is pair-production (Figure 3.1). The measurement is to be made in a very high background of charged particles as well as a significant background of neutral induced events and albedo gamma-rays; this requires a picture-type detecting apparatus, to identify the pair-production event and study its properties. At present there are four types of imaging devices that might be considered: the cloud chamber, bubble chamber, nuclear emulsion, and spark chamber.

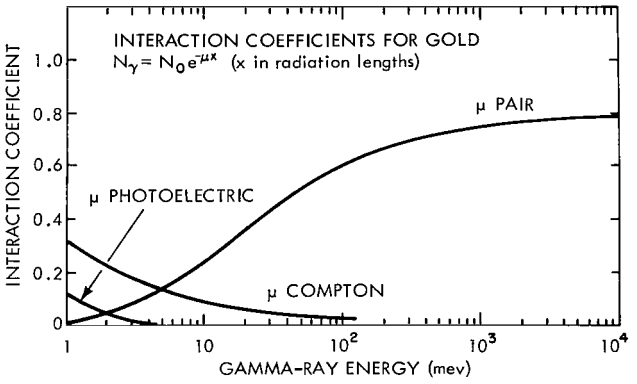

Figure 3.1—Gamma-ray interaction coefficients for gold. The data are taken from Rossi (1952, pp. 77-86).

The cloud chamber and bubble chamber are not adaptable to space flight (though one cloud chamber electron experiment has been flown successfully on balloons—Earl, 1961). Both are heavy and bulky and extremely sensitive to the environmental extremes encountered in space flight. Worse still is their excessive dead time and the bubble chamber's lack of trigger capability. The nuclear emulsion has been used with some degree of success in gamma-ray astronomy in several experiments (Rossi, 1952, pp. 77-86; Svensson, 1958, p. 347; Bracessi and Ceccarelli, 1960; Klarmann, 1962; Fichtel and Kniffen, 1965; and Frye, Reines, and Armstrong, 1966) but this device lacks time resolution, being continuously sensitive from the time of manufacture until development. This results in a large background of both charged particles and gamma-ray-induced pairs, making the nuclear emulsion suitable only for searching for point sources and then only when accurately oriented so that the solid angle subtended at the emulsion by the source is small. Though emulsions offer good spatial resolution, this technique has reached its useful limit for balloon flight experiments except when used in conjunction with some device to provide time discrimination. For satellite experiments, in addition to the need for recovery, emulsion experiments must cope with the very high background accumulation from trapped radiation as the spacecraft passes through the belts.

The remaining imaging detector now available for application to space research is the spark chamber. In principle, a properly designed spark chamber can meet all the requirements of a good gamma-ray detector: to provide a pictorial image of the pair production (a protection against phenomena with a false resemblance to gamma-rays); to give reasonable angular resolution of incoming gamma-rays; to offer a large solid angle to detect ambient radiation over large regions of the sky; to provide energy resolution by observing the pair opening angle and multiple scattering of the electrons; and to give accurate time resolution. For these reasons a spark chamber was chosen for the detector in this experiment.

As explained later, it will ultimately be necessary to practice gamma-ray astronomy from satellites. Since most scientific satellites are non-recoverable, photographic chambers are essentially eliminated. Of the remaining types of spark chambers, a direct digital readout device requires the least amount of on-board data handling and thus is more reliable, weighs less, and takes up less room. Also, a digital device does not need an optical path between the plates through which to view the sparks; this allows narrower plate spacing. A narrower gap has several advantages. Spark formation needs less applied voltage, and need not have the energy to provide a photographic image; this means lower power requirements and less electrical noise. More spark modules may be stacked in a given height; this gives more track information for a given opening angle of the detector. For these reasons, a digitized wire-grid spark chamber was chosen for this balloon experiment—which is to serve as a first-generation phototype for an eventual satellite experiment.

The digitized spark chamber has several other advantages over photographic types, even in balloon experiments. There is no need to carry large amounts of film. There is a built-in fiducial system; this does not require the careful attention that must be given to alignment of mirrors when installing a fiducial marking system, as with optical-type chambers. Finally, there is little "spark robbing," a phenomenon that often occurs in optical-type chambers when an electron pair is recorded. Such robbing occurs when more energy is dumped in one spark (presumably the one which reaches breakdown first) than in the other, rendering the latter unobservable by optical imaging.

The following sections deal with the stages of development that led to the adoption of the final flight configuration of the digitized wire-grid spark chamber.

2. Module Development

The basic element of the spark chamber is the spark module. The early development of the spark chamber to be used for this experiment began with a detailed study of the operating characteristics of the individual module. The original concept as pictured in Figure 3.2 had a six-inch-square active area consisting of a wire-grid anode on either side of a negatively pulsed cathode plate, with a plate-to-wire separation of 2.36 millimeters.

The wire grid consists of 128 parallel 0.18-mm beryllium-copper wires, separated by 1.1 mm. Each wire is held under 20-ounce tension and is ultrasonically welded and soldered to copper pins

imbedded in terminal strips epoxied to both ends of the frame. The frames are machined from glass-bonded mica, which was chosen for its low-outgassing properties; this was to minimize gas contamination for long-term operation without the need for flowing gas. At one terminal strip the wires are terminated at the pins; at the opposite terminal the wire continues past the pin, is passed through the ferrite memory core, and is attached to one side of a resistor, R_w. A lead passes from the other side of the resistor to a common ground strip. The core readout scheme will be discussed later in this chapter; basically, the core is set when a spark occurs and current flows from ground through the core and the spark to the plate. This occurs on both sides of the plate and, since the grids are orthogonal, both an x and y coordinate track location are obtained for each module.

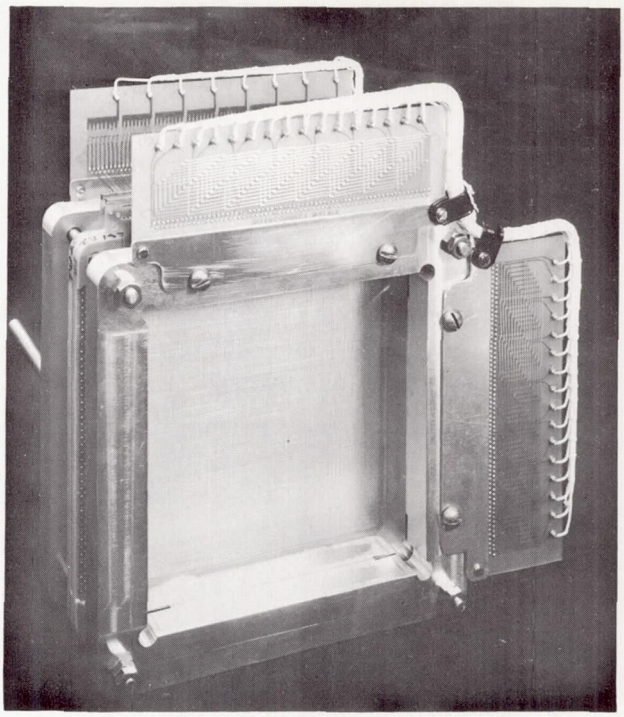

Figure 3.2—Preliminary design of spark module, with one plate sandwiched between two grids. Sparks occur between grids, at ground potential, and plate at high negative potential.

To discuss the choice of spark gas mixtures needs a brief review of the spark discharge mechanism. An energetic charged particle passing between the plates of the chamber will produce, by ionization along its trajectory, $N_0 p$ electrons per centimeter, where N_0 is the number of electrons produced per centimeter at 1 atmosphere, and p is the number of atmospheres. These electrons are then accelerated in the applied field V_p/ℓ, producing additional electrons at a rate given by Townsend's first ionization coefficient (Meek and Craggs, 1953, pp. 11-12), per centimeter, until, at a distance x from the point of the original electron, $e^{\alpha_T x}$ electrons have been produced. Since the electrons move much more rapidly in the applied field than the ions, a space charge field E_r is created. According to Raether (1964, pp. 78-79), and Meek and Craggs (1953, pp. 255-257), with a sufficiently high applied field this process continues until the space-charge field (which augments the applied field in the region of the avalanche head) is comparable in magnitude to the applied field. At this point, the field at the center of the avalanche head is significantly reduced, and recombination due to the high density of electrons and ions present at that point leads to secondary photons. The photons produce photoelectrons in the gas surrounding the avalanche; this leads to more avalanches, particularly along the axis of the original avalanche where the field is enhanced. In this manner a self-propagating streamer occurs with sufficient ion-electron density to maintain current flow until the applied voltage is removed. The number of secondary electrons $N = e^{\alpha_T x_c}$ required to produce a streamer seems to be of the order of 10^9, hence $\alpha_T x_c \approx 20$. This value of N required is extremely uncertain and depends to a large extent on the parameters of the particular spark chamber, but $\alpha_T x_c$ is quite insensitive to N and may be considered a constant. The quantity x_c, as defined above, is termed the "critical distance" for streamer formation and must be less

than ℓ, the gap width, if a streamer is to be formed. In fact, it is the excess of ℓ over x_c that determines the spark efficiency given by

$$\eta = 1 - e^{N_0 p(\ell - x_c)} .$$

Clearly, to obtain maximum efficiency it is necessary to maximize N_0 and p and minimize x_c. Since $x_c = 20/\alpha_T$, a gas should be chosen with maximum α_T, but, for a spark to occur at all α_T must be greater than $20/\ell$. For small gap separations such as the 2.36 millimeters used in this chamber, a gas must be chosen with the maximum possible α_T. Fortunately a Penning mixture (Druyvesten and Penning, 1940) of neon with one percent argon has an α_T of about 200 cm^{-1} or more (much higher than the 42 cm^{-1} of neon alone), providing reasonable spark efficiencies in the present chamber with peak applied voltages of the order of one or two kilovolts. Because of the availability and cost, a mixture of 90-percent neon and 10-percent helium is used in place of pure neon. Testing various gas mixtures has failed to improve upon this mixture except for an addition of one-half to one percent ethanol to suppress spurious (non/particle-track-associated) sparking by absorbing stray photons.

Figure 3.3a shows the simplified pulser circuit used for pulsing the plate. The development program consisted of operating the basic modules while varying the gas mixture; the applied high voltage; and components R_w, R_ℓ, R_0 and C_0—to obtain optimum spark characteristics. The desirable characteristics include high single and multiple spark efficiency, low spark spreading (spreading refers to the number of cores set per spark), high x-y efficiency (sparks where at least one x and one y core are set), and low spurious sparking. Analyzing the circuit in Figure 3.3a gives a reasonable approximation to the high voltage-time profile appearing on the plate:

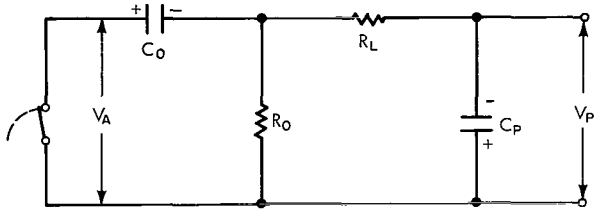

(a) Charging circuit

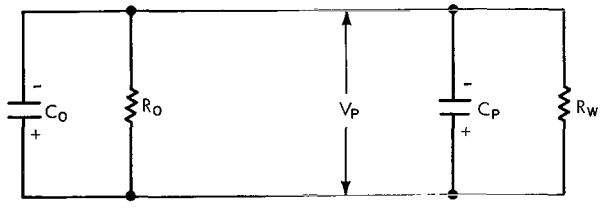

$R_L \ll R_w$

(b) Discharging circuit

Figure 3.3—Simplified charging and discharging circuits with V_A the applied high voltage, C_0 the charging capacitor, R_0 the charging resistor, R_ℓ the tuning resistor, C_p the module capacitance, R_w the wire termination resistance, and V_p the resultant voltage appearing across the spark gap.

$$V_p(t) = \frac{V_A}{C_p R_\ell} \frac{1}{\alpha_- - \alpha_+} \left(e^{-\alpha_+ t} - e^{-\alpha_- t} \right) ,$$

where

$$\alpha_\pm = \frac{1}{2} \left[\left(\frac{R_\ell + R_0}{R_0 R_\ell C_0} + \frac{1}{R_\ell C_p} \right) \mp \sqrt{\left(\frac{R_\ell + R_0}{R_0 R_\ell C_0} + \frac{1}{R_\ell C_p} \right)^2 - \frac{4}{R_\ell R_0 C_0 C_p}} \right]$$

and resistances are in ohms, capacitances in farads, and time in seconds. V_A is the high

voltage applied to the anode of the pulser tube, V_p the resultant voltage appearing on the plate, and C_p the measured capacitance of the module. Figure 3.4 shows some calculated voltage profiles for typical operating parameters. The actual voltage pulses vary somewhat from the curves because of stray inductances. For the most part this results in slightly longer rise times than calculated, and in some ringing.

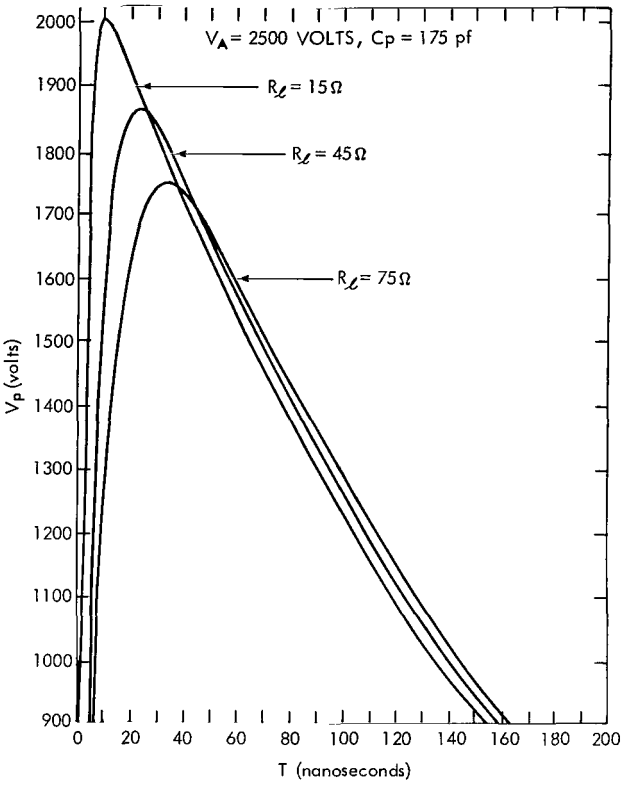

Figure 3.4—V_p vs time for three typical sets of circuit parameters.

The circuit parameters shown in Figure 3.3a were chosen so as to optimize the voltage profile appearing on the plate. The nature of the circuit is revealed more clearly by analysis for $R_\ell = 0$. This gives

$$V_p = V_A \left(\frac{C_0}{C_0 + C_p} \right) e^{-t/R_0 (C_0 + C_p)} .$$

Thus the circuit acts simply as a capacity voltage divider; since R_ℓ is rather small, this is not a bad approximation for $R_\ell \neq 0$. Since C_p is fixed (specifically measured to 400 pf for the module described above) it is advantageous to make C_0 as large as possible relative to C_p, consistent with fast rise times. A value of 1000 pf is used. This is perhaps somewhat low for the module considered here but, as will be seen, modules are now being used which have a still lower C_p. C_0 must, of course, be large enough to give the spark enough energy to set the cores; 1000 pf easily satisfies this criterion, since only about 0.003 joule is required to set a core. R_ℓ (never more than a few ohms) is used to tune the circuit for the desired voltage profile and peak voltage, once the other parameters have been selected on the basis of the other given factors. Figure 3.4 shows how V_p is affected by changing R_ℓ, the other parameters being constant. The value of R_0 is chosen so as to allow the voltage pulse to remain on the plate for a long time compared with the spark formation time (about 60 nanoseconds), but if R_0 is too large, spurious sparking, spark spreading, and edge breakdown will be enhanced (150 ohms has been found quite satisfactory).

The simplified pulser circuit does not show R_w since 128 of these resistors in parallel have very little effect on the voltage pulse shape; but they play a very important part by increasing multiple spark efficiency once a spark has occurred. The problem of multiple spark efficiency exists because of jitter in the spark formation time due to statistical fluctuations in the avalanche formation. Such a jitter causes one spark breakdown to occur before another, even when the primary ionization is produced simultaneously, as in the case of an electron pair. Schneider (1963) has calculated this time jitter for various numbers of ion pairs produced in the gap. Observations have shown that, for the module considered here, the maximum efficiency,

given by $\eta = 1 - e^{N_0 p \ell}$, is about 85 percent. This gives $N_0 p$ as about 8 ions per centimeter. The average number of ion pairs formed in a gap, ℓ, is given by $\langle n_e \rangle = N_0 p \ell \approx 2$. Schneider's results give $\Delta\bar{\tau}/\bar{\tau} = 0.15$, where $\bar{\tau}$ is the average normalized spark formation time defined by $\bar{\tau} = t_{sf}/t_0$. Here t_{sf} is the actual spark formation time, which according to Fischer and Zorn (1961) is about 60×10^{-9} seconds for this case, and t_0 is the mean time between ionizing collisions. Hence $\Delta\bar{\tau} = \Delta t_{sf}/t_0$; therefore $\Delta t_{sf} \approx 0.15\ (60 \times 10^{-9})$ seconds = 9 nanoseconds. The discharge circuit in Figure 3.3b, if $R_\ell << R_w$, gives

$$\text{Discharge time} = \tau_d = (C_0 + C_p)\left(\frac{R_0 R_w}{R_0 + R_w}\right).$$

Table 3.1 gives values of Δt_{sf} for different values of C_p and R_w (with C_0 = 1000 pf, and R_0 = 150 ohms). For the module under consideration, C_p = 400 pf, so R_w should be at least 56 ohms to give a long voltage decay time as compared with the 9-nanosecond multiple-spark jitter time.

The module design so far discussed did not give a reasonable x-y efficiency, no matter what circuit parameters were chosen. Because of the jitter in spark formation time, the spark that forms first on one side of the plate tends quickly to drain the charge in the vicinity of the spark, effectively reducing the field on the opposite side of the plate. In practice, this severely reduces the probability of spark formation on the opposite side. The maximum x-y efficiency obtainable is about 60 percent. For this reason a module using wire planes for both the anode and the cathode was developed.

Figure 3.5 shows a wire-grid to wire-grid module constructed in the same manner and using the same frames as before, with the two grids strung orthogonal to each other on opposite

Table 3.1

Mean Difference in the Spark Formation Time for Two Simultaneously Produced Tracks.

C_p (picofarads)	R_w (ohms)	Δt_{sf} (nanoseconds)
400	10	14
400	56	57
400	100	84
175	10	11
175	56	48
175	100	70
C_0 = 1000	R_0 = 150	

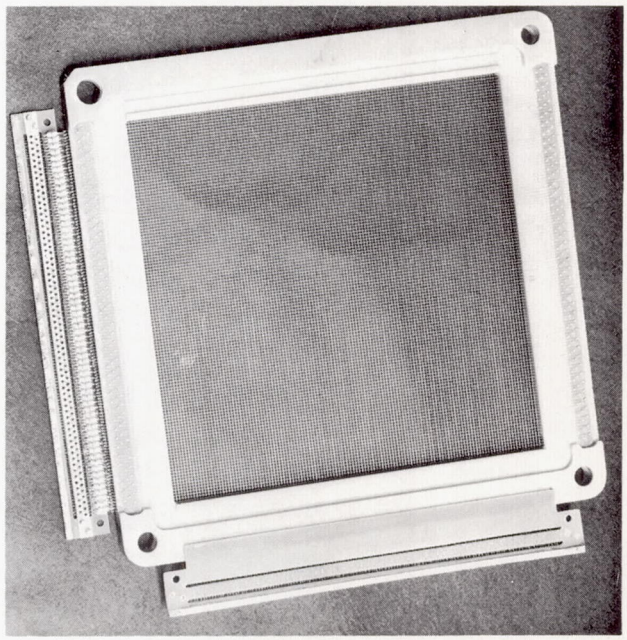

Figure 3.5—Wire-wire spark module with core trays mounted along two sides. Spark discharge occurs between wire planes. The planes consist of 128 parallel wires, orthogonal to wires on the opposite side of the frame.

sides of one frame, giving a 2.24-mm spark plane separation. A problem immediately arises: the high voltage must now be carried to the high-voltage grid by leads that pass through the ferrite memory cores. As will be discussed in the section describing the readout scheme, two additional leads at ground potential that connect to the readout electronics must also pass through the 0.76-mm-diameter core orifice. The high voltage must not appear in the electronic circuits, or component failures will result. Using Nyclad insulated wire and carefully potting the core orifice with silicone potting compounds appears to be sufficient to prevent such breakdowns, even in a neon environment. Another possible mishap is the false setting of cores as the high voltage is applied to the grid; fortunately, the 0.1 ampere flowing through a given core for the 15-nanosecond pulse rise time is well below the threshold for setting a core (about one ampere flowing for one microsecond).

The attractive feature of this type of module is that the spark current flows from the ground bus, through a core on the grounded grid to the high-voltage rigid, through a core on the high-voltage side to the high-voltage bus. Thus the spark current is continuous through cores in both decks, which ensures a 100-percent x-y efficiency. With this problem eliminated, R_w can be made large enough to ensure a high multiple efficiency, though the tendency for increased spreading limits the value to about 100 ohms. Figures 3.6 and 3.7 show results obtained in module testing at a series of applied voltages and pressures, with R_w equal to zero and 100 ohms, respectively. In both cases the gas mixture consists of 89.5-percent neon, 9.9-percent helium, 1.0-percent argon, and 0.5-percent alcohol (by pressure). For a given pressure, the applied voltage should be maintained slightly above the efficiency knee at the beginning of the plateau, since spark spreading reaches no such plateau, at least within the range of applied voltages tested. Figures 3.6 and 3.7 show that the highest efficiency and lowest spreading are obtained when $R_w = 0$; however, as already explained, 100 ohms is used to maintain the high multiple spark efficiency needed for observation of electron pairs.

The circuit parameters applicable to the wire-grid to wire-grid module are C_0 = 1000 pf, C_p = 175 pf, R_w = 100 ohms, R_0 = 150 ohms, and R_ℓ = 22 ohms. Thus the applied voltage profile and spark formation time jitter may be obtained from Figure 3.4 and Table 3.1. The 175-pf C_p applies to the case where gold plates

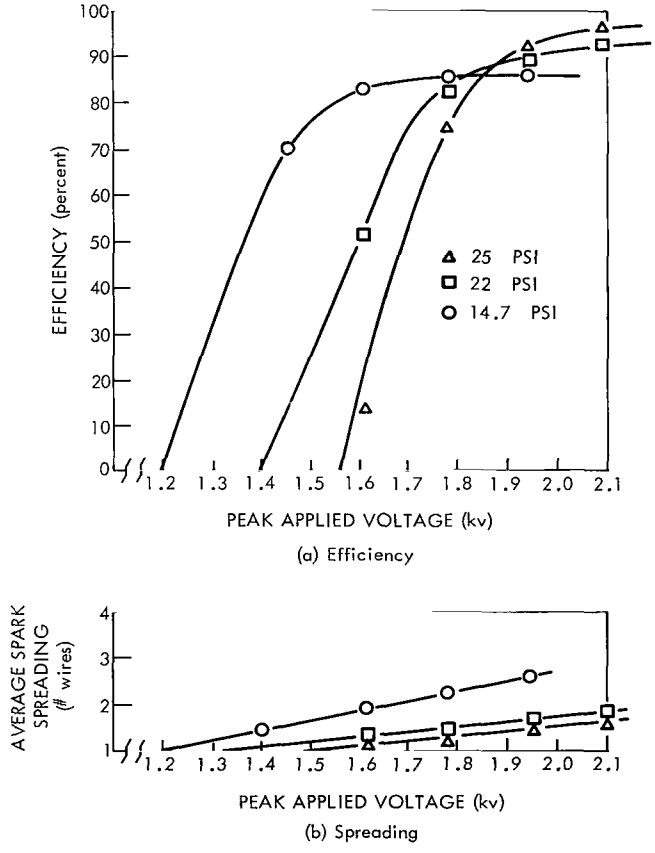

Figure 3.6—Efficiency and spreading as a function of peak applied voltage for a module with no wire termination resistors.

are placed on either side of the module, 2.36 mm from the grids, and left floating electrically. This is the situation in the assembled detector, as described below.

3. Detector Assembly

The spark-chamber assembly consists of a stack of 30 individual wire-grid two-coordinate (x-y) modules. Because of the obvious ambiguity of properly associating two or more x readings with the proper y readings, two of the modules contain wires arranged at 45 degrees with respect to the wires in the remaining modules. The 45-degree grid module consists of a grid-plate module, in preference to the wire-grid to wire-grid modules used on the 30 x-y grids.

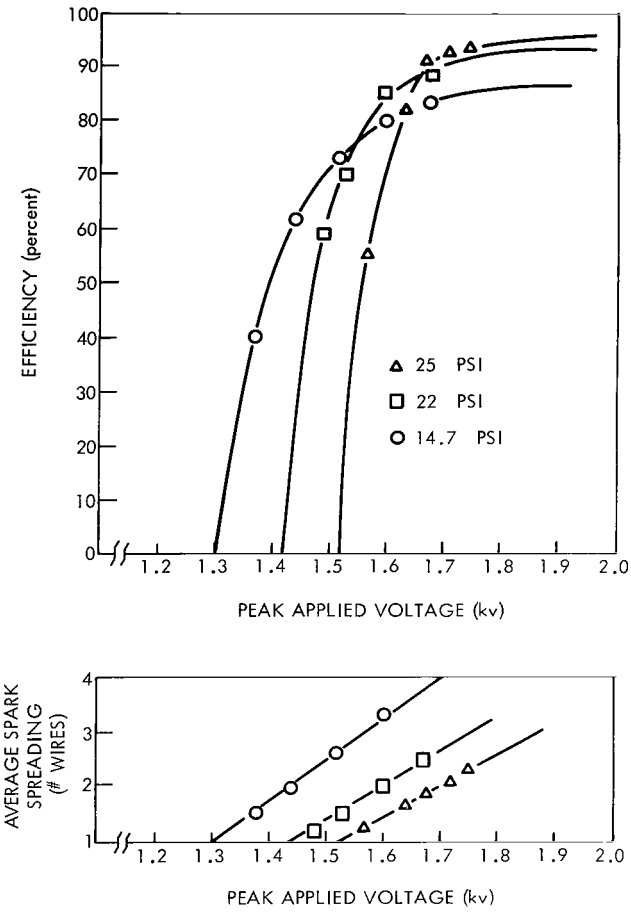

Figure 3.7—Efficiency and spreading as a function of peak applied voltage for a module with R_w = 100 ohms.

Between each module is placed a pair converter consisting of 0.02 radiation length of gold plated on a structural layer of 0.18 mm (0.002 radiation length) aluminum. Using many thin converters allows observation of the created pair near the apex, before their passage through large amounts of scattering material. This arrangement retains a maximum of information on the arrival direction of the gamma-ray, together with enough high-Z material to provide pair conversion. Furthermore, once the pairs are formed, the plates may be used as scattering cells to obtain information on the electron momentum and hence the energy and arrival direction of the parent γ ray. The next chapter will discuss the quantitative details of the scattering.

The total of 32 active spark modules and 30-pair-converting plates is divided into two identical spark chamber units of 16 spark modules and 16 plates, each with a 45-degree grid on the bottom. The two units are stacked one above the other and separated by a thin (4.78 mm) 15.24-cm square Pilot B plastic scintillator, which is used as one element of the triggering telescope. A quartz-faced Čerenkov tube, 12.7 cm in diameter, is placed beneath the bottom chamber to complete the telescope. The photo cathode of the Čerenkov tube has a radius of 10.2 cm which defines the area of the bottom element of the telescope.

Figure 3.8 shows the assembled detector. Many of the support components to be described in later sections are mounted on the side of the detector. These include the high-voltage pulsers,

magnetic core trays, central scintillator light pipe, and the sense amplifier and shift register circuits used in the readout. Mounted beneath the detector is most of the readout electronic circuitry.

The entire chamber (excluding the Čerenkov detector and the electronics below it) is hermetically sealed within a stainless-steel cylindrical container with a hemispherical dome. The spark gas is confined within this shell, which is designed to withstand pressure differentials of up to at least two atmospheres because of the near vacuum at balloon-flight altitudes. A thin (0.508 mm) aluminum port, 12.7 cm in diameter, in the bottom plate provides a window through which the Čerenkov detector may view the chamber area. In addition, two hermetically sealed bulkhead connectors provide for interconnecting electronic leads through the interface. Finally, a port in the bottom bulkhead plate provides for evacuating and filling the internal chamber with spark gas.

The entire chamber and container are surrounded by a Pilot B plastic scintillator dome, 16-mm thick, which is viewed by six phototubes. The output of the dome is placed in anticoincidence with the coincidence telescope to guard against incoming charged particles. Figure 3.9 shows schematic view of the detector assembly with the anticoincidence dome.

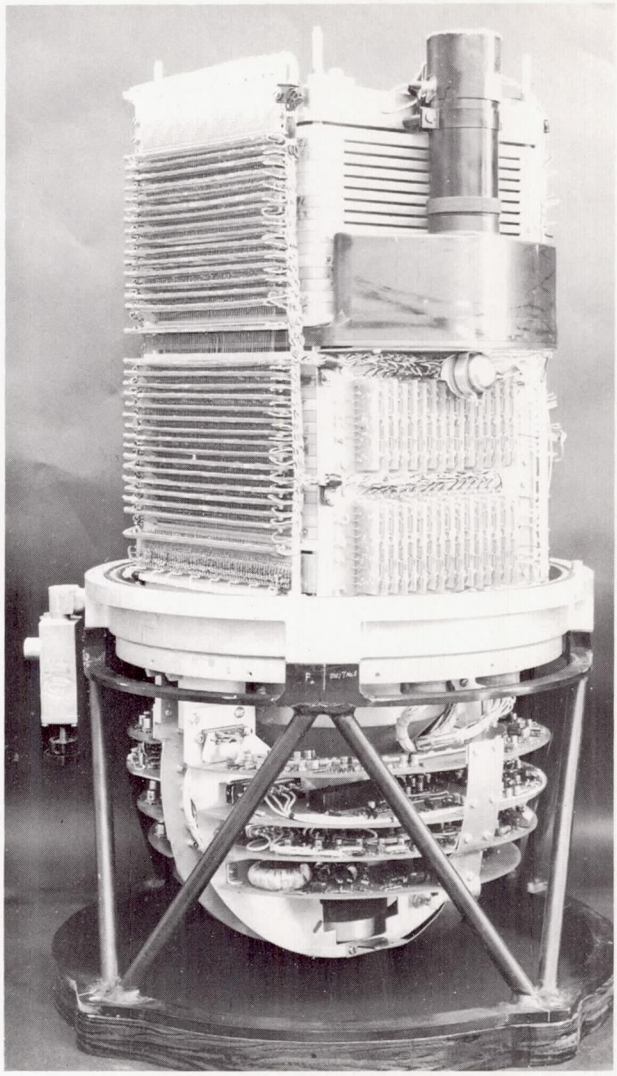

Figure 3.8—Assembled spark chamber.

Several kinds of events might falsely trigger the anticoincidence-coincidence conditions. The most likely is the possibility of a leak in the anticoincidence dome, allowing charged particles to pass through the telescope and trigger the chamber. The anticoincidence counter must have extremely high efficiency, since the ratio of the charged-particle intensity to the gamma-ray intensity at typical balloon altitudes and latitudes is of the order of 10^3. Laboratory tests have shown the efficiency for anticoincidence to be at least 10^{-4}, and flight data have shown it to be better than that. Other false triggers might be provided by: (1) electrons resulting from the decay of muons whose lifetime exceeds the anticoincidence gate, (2) downward scattering of low-energy electrons penetrating upward through the bottom which is unprotected by anticoincidence, and (3) neutral inducted interaction secondaries—charged particles and gamma-rays—produced within the anticoincidence shield. All of these contributions can be eliminated by careful analysis of the pictorial

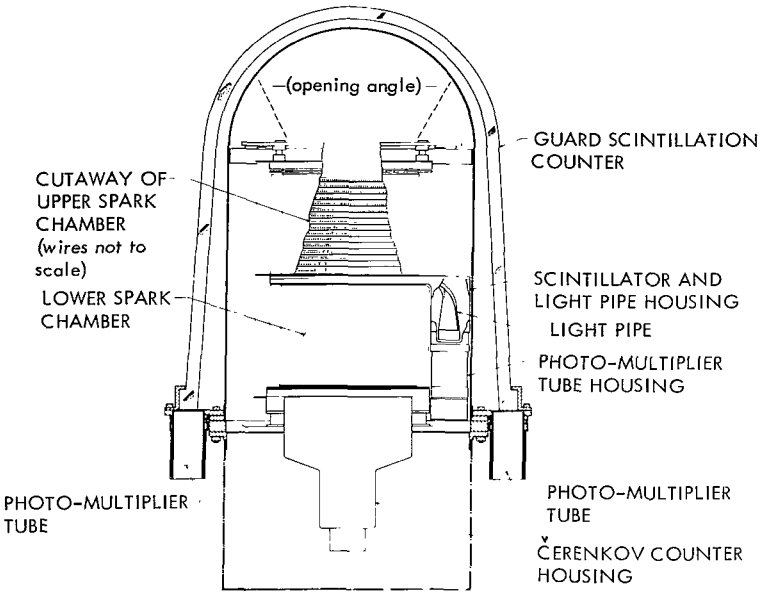

Figure 3.9—Complete detector assembly.

spark-chamber presentation. The main necessity is to minimize false triggers and hence maximize detector live time. The most serious contribution to detector dead time is the type-(3) event.

The energy and direction of arrival of the incident gamma-ray that produces the observed pair are obtained by analyzing the vector momentum of the pair. It is necessary to know the pair production efficiency of the detector, the mean angle of scattering of the electrons, and the distribution of energy in the two electrons. These processes and their measurement will be discussed in the next chapter. It will be shown that each of these combines to reduce the angular resolution and detection efficiency as the energy of the primary photon is reduced. However, since energy can be at least roughly determined, these effects may be separated into energy bins, where the sensitivity and accuracy of the measurements increase with energy.

4. On-Board Data Handling System

The data system consists of a buffered memory readout system, a housekeeping data handling system, and a tape multiplexer and recorder. Each of the 30 wire-grid decks contains 256 cores; also, each of two 45-degree grids contain 128 cores. This makes a total of 7936 cores to be read out. Each core is threaded by three wires: the spark wire, previously mentioned, which carries current to set the core; a reset wire, threading 32 cores, one per module, and carrying current to reset the core; and a sense wire, threading all 256 cores of one module, and sensing a core change of state. Figure 3.10 shows the three-dimensional readout scheme.

Each of the current sources provides a 0.8-ampere, 1-microsecond pulses through one of 16 columns of cores selected by the grounding-circuit select system. Hence, by means of one selected current pulser and one selected grounding circuit, the contents of a column of 32 cores are coupled to their associated sense wires. These sense wires are, in turn, transformer-coupled to 32 sense amplifiers which detect the 0.5-volt output pulses from the set cores as they are reset. The output of the sense amplifiers is then transferred to a 32-bit shift register.

The readout is initiated by an output from the anticoincidence-coincidence telescope. A millisecond delay allows the spark transients to die away; then all scalers are set to zero, the shift

register is cleared, the first reset wire is fired, and the outputs of the first column of cores is loaded into the shift register. As depicted in Figure 3.11, shift pulses are counted until a set core is found; at this point, counting and shifting are inhibited until the core address is recorded. After 32 shift pulses, the second wire is fired and the outputs of the second column of cores is stored in the shift register. The process repeats until all cores are examined. The shifting occurs at a rate of 8192 cores per second, and on the average an additional 1/28 second is required to record the address of a set core. Hence the total time required to read out an event in which n_c cores are set is $(1 + n_c/28)$ second. In a typical event in which 84 cores might be set, 4 seconds would be required to read out and record the event.

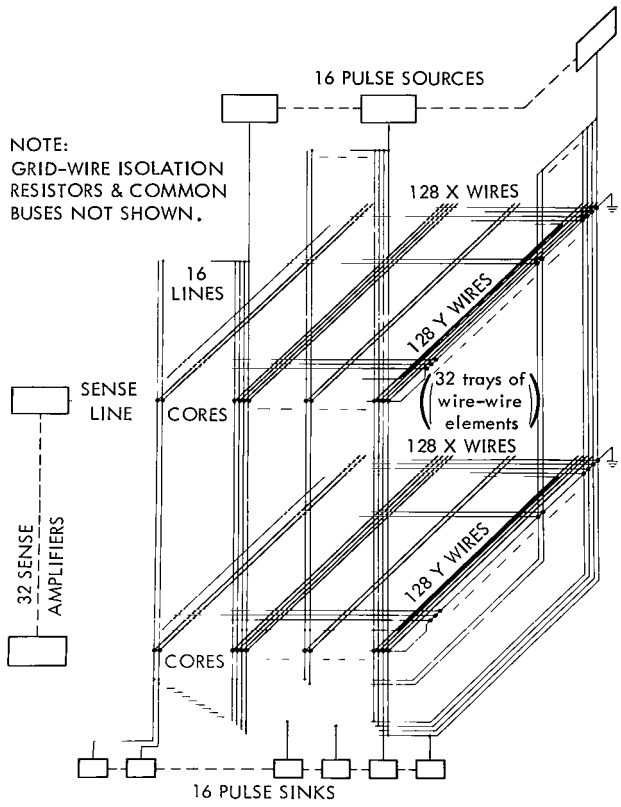

Figure 3.10—A three-dimensional representation of the core readout scheme.

During the readout time, the chamber is inhibited against further coincidence signals until the entire core array has been read out and recorded. Thus readout time represents dead time for the chamber. Since the neutral-particle event rate at ceiling is about one count per second, the live time is only about 22 percent of the elapsed time; a somewhat low but acceptable value. The live time for future flights will be increased as follows: the solid angle of the coincidence telescope will be restricted so that particles entering the detector opening angle are accepted but particles resulting from neutral particle interactions in the side walls are rejected. Also, excess material at the top of the detector, which might produce such unwanted neutrals, will be eliminated.

It is also desirable in aiding the analysis to record other peripheral data, herein called "housekeeping" data. Table 3.2 lists the 16 housekeeping parameters recorded, together with the associated accuracy. Both digital and analog data are recorded. The system provides eight channels of digital pulse counting and an eight-position analog multiplexer and analog-to-digital converter.

The binary accumulators are 8 bits in length, providing counting accuracy of one part in 256. In three rates, digital prescalers are provided to scale down counting rates so that the accumulators will not overflow during the counting interval. One of the accumulators serves as a live-time counter, which counts elapsed time but is inhibited while the detector is being read out. The analog-to-digital converter is also accurate to one part in 256; monitors voltage transducers for the temperature and pressure functions.

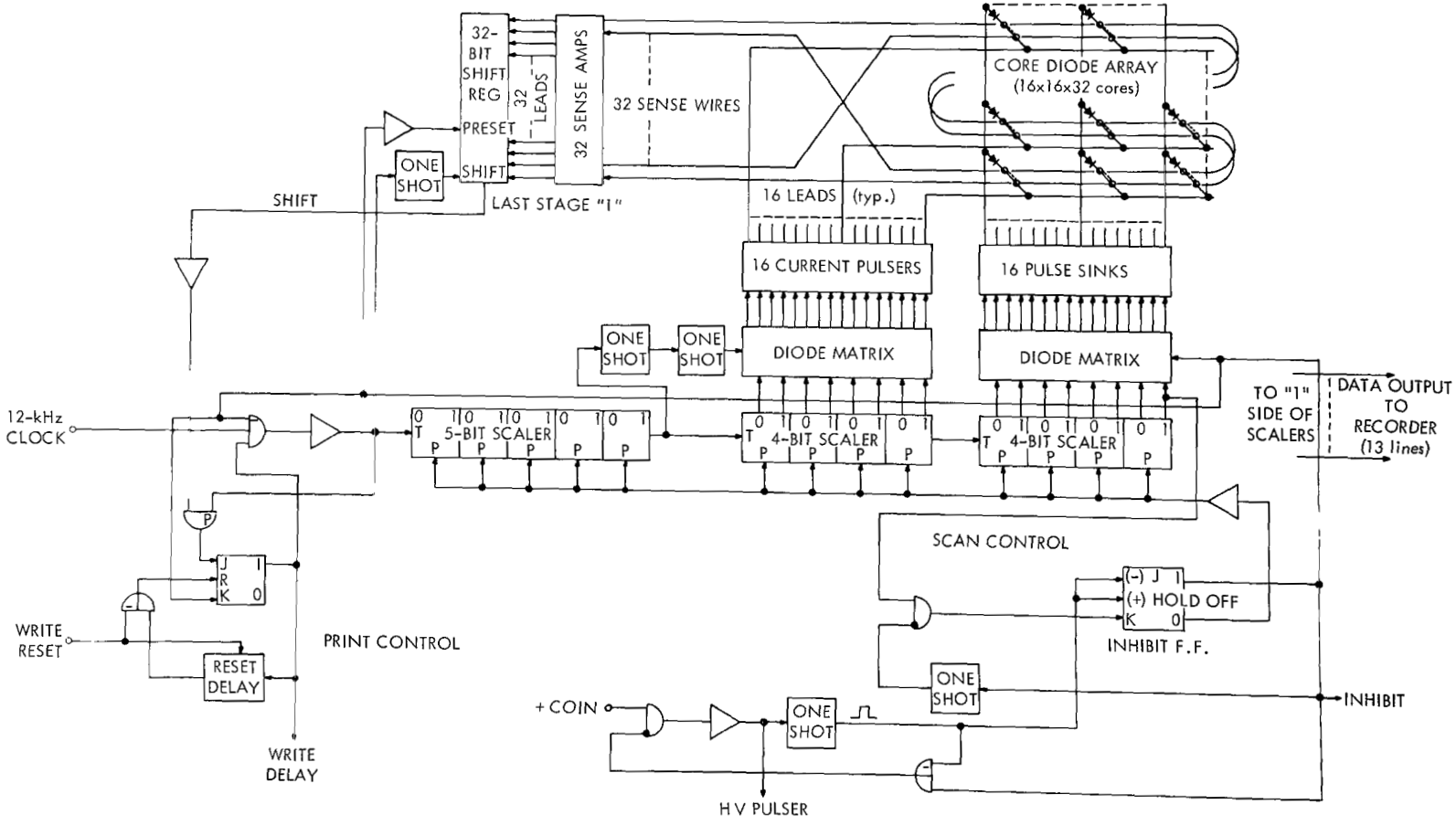

Figure 3.11—Memory system block diagram.

Table 3.2

Spark-Chamber Housekeeping Channel Allotment.

Channel Number	Subcommutation Number	Parameter	Maximum Rate (rates) Accuracy (analog) (counts per second)
0		A Counter rate	65,536
1		B Counter rate	1,024
2		C Counter rate	1,024
3		$\overline{A} \cdot B$ rate	256
4		$\overline{A} \cdot B \cdot C$ rate	256
5		$B \cdot C$ rate	256
6		$\overline{A} \cdot C$ rate	256
7		Detector live time	All analog parameters are recorded with an accuracy of one part in 256.
8		Course magnetometer	
9		Fine magnetometer	
10		Jet time (on-time)	
11	0	A-dome phototube temperature	
	1	Ambient temperature	
	2	Chamber temperature	
	3	Electronics temperature	
12		Pendulum magnetometer	
13		Rate gyro	
14		Orientation gas pressure	
15	0	Spark chamber gas pressure	
	1	Battery voltage	
	2	Heater voltage	
	3	Heater current	

Data is logged in parallel into a special 16-track data recorder developed for balloon-flight work at the Goddard Space Flight Center. The recorder runs continuously at 0.355 inch per second and carries enough tape to handle 14 hours of data collection (recorded on the tape at 32, 16-character words per second). For 3 seconds, spark-chamber memory-core data are recorded alone; during the fourth second, the system alternates housekeeping words and data words so that a full set of the housekeeping data is recorded every fourth second. Table 3.3 gives the format in which the data are recorded. The core words are 14 bits in length, 13 being for core address and 1 for a scan-ready mode indicator. The housekeeping words are 14 bits in length, including 8 data bits, 4 bits of channel address, and 2 bits of subcommutator indicator for the 2 channels that require less frequent intervals of recording and hence are subcommutated. Figure 3.12 is a simplified block diagram of the entire data handling system.

Table 3.3

Spark-Chamber Tape-Track Allotment.

Track No.	Housekeeping	Spark Data
1	Data 2^0	Column No. 2^0
2	Data 2^1	Column No. 2^1
3	Data 2^2	Column No. 2^2
4	Data 2^3	Column No. 2^3
5	Data 2^4	Column No. 2^4
6	Data 2^5	Column No. 2^5
7	Data 2^6	Column No. 2^6
8	Data 2^7	Column No. 2^7
9	Identification strobe	---
10	---	Identification strobe
11	Channel No. 2^0	Wire indicator
12	Channel No. 2^1	Row No. 2^4
13	Channel No. 2^2	Row No. 2^3
14	Channel No. 2^3	Row No. 2^2
15	Subcommutation No. 2^0	Row No. 2^1
16	Subcommutation No. 2^1	Row No. 2^0

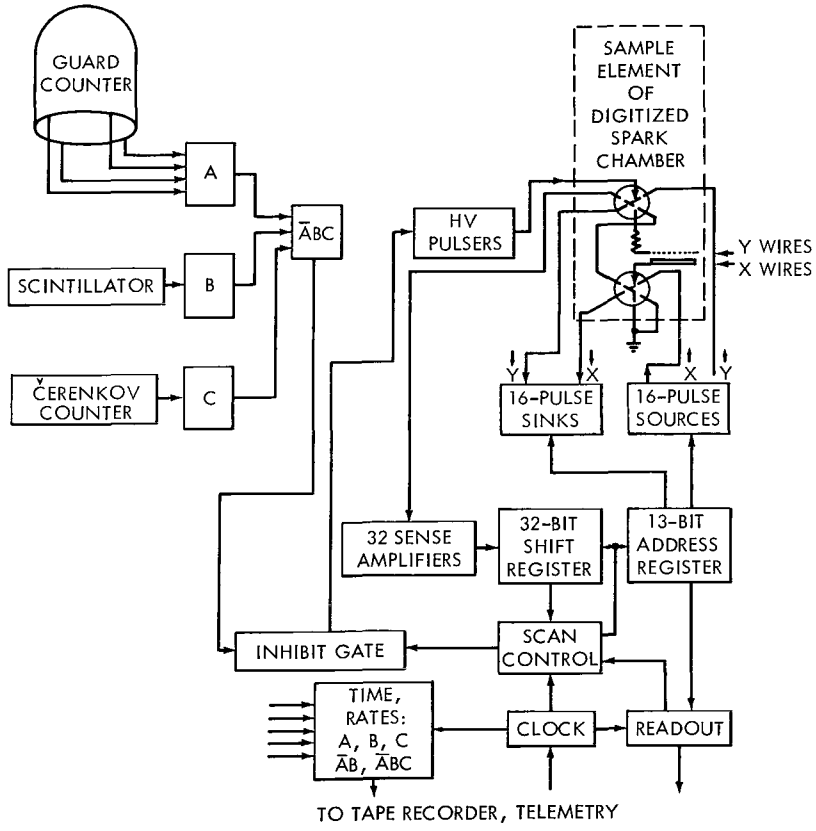

Figure 3.12—Simplified block diagram of the entire data handling scheme.

When a flight tape is obtained, it is run through a data processor and a buffer system to convert the data to seven-track, odd parity, high-density tape suitable for input to an IBM 7094 computer. Computer programs then provide a pictorial display of each spark event, including the time of the event. In addition, a complete listing of the housekeeping data is obtained. Figure 3.13 is an actual printout of a typical gamma-ray event, obtained from the computer output. Chapter IV describes the data analysis.

The data system is completed by a compact ground station that allows readout of housekeeping data and spark event, in real time on the ground and from magnetic flight tape in the field. This station checks the proper functioning of all components of the system before a balloon flight.

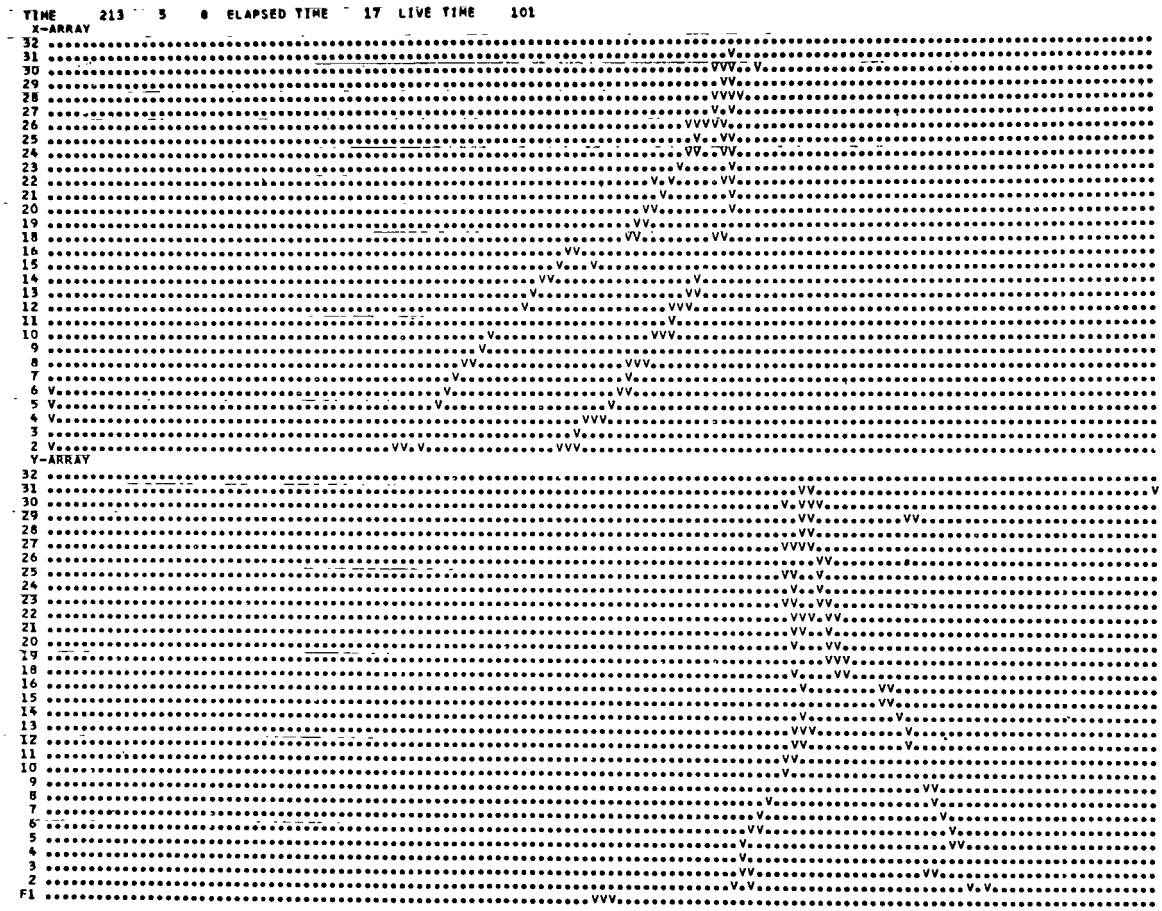

Figure 3.13—Spark chamber computer printout of a typical gamma-ray event, including the readout of the x and y projection. The vertical axis is compressed by a factor of 5.05 with respect to the horizontal axis.

5. Coincidence Telescope and Logic Electronics

As previously stated, the coincidence telescope consists of a scintillation counter separating the upper and lower chamber, and a Čerenkov detector beneath the lower chamber. The central

thin scintillator is viewed from one edge by an RCA C-7151H photomultiplier through a light pipe made from six strips of plexiglass, which are heated and individually formed into a right-angle below, then bonded to the scintillator. Such a light pipe was found to be twice as efficient for light transmission as a one-piece "adiabatic" light pipe. The Čerenkov tube is an EMI Type 9530QS photomultiplier, 12.7 cm in diameter with a quartz face one centimeter thick which acts as a Čerenkov radiator, and a ruggedized dynode structure for protection in the rigorous environment of balloon and space flight. The quartz face of the tube is coated with Lux-sorb to absorb upcoming light from the quartz radiator and thus provide discrimination against upcoming charged particles in the region not protected by the anticoincidence dome. The bell-shaped anticoincidence dome is loosely wrapped with aluminum foil before a light seal of black epoxy is applied to its surface; it is viewed from the bottom by six gain-matched RCA C-7151H photomultipliers, whose output charges are summed to provide the anticoincidence signal

Each of the photomultiplier tubes described above has its own compact and self-contained high-voltage supply, making it unnecessary to rout high-voltage leads throughout the detector system. In each case the tube and power supply are placed in a hermetically sealed container to prevent corona. The only input required is a 28-vdc power source and a return ground path.

For the anticoincidence dome, with six phototubes, this ensures so that the failure of one power supply will not seriously affect the signal output.

Figure 3.14 is a block diagram of the coincidence circuit. The output charge signals from each element in the counter telescope are amplified and fed into an amplitude discriminator. The output of each discriminator generates a gate signal 100 nanoseconds wide. An additional

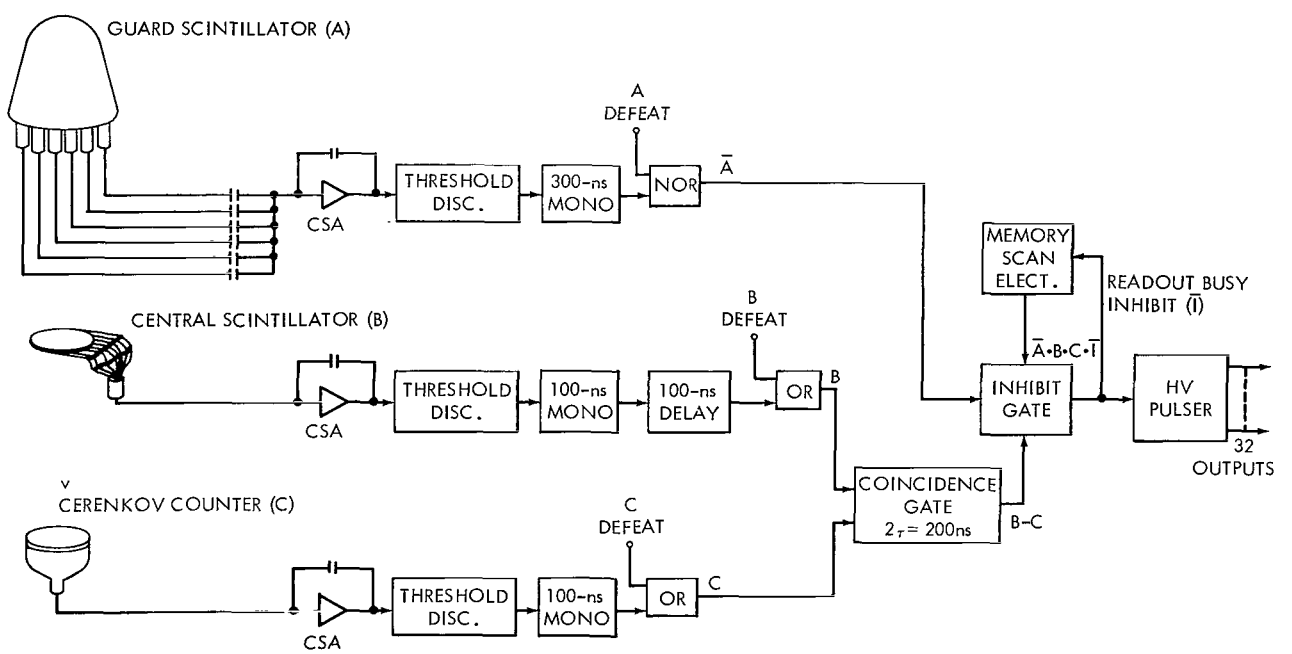

Figure 3.14—Block diagram of the coincidence circuit.

100-nanosecond delay is applied to the central scintillator output to compensate for the long delay time of the large C counter phototube. The B and C outputs are then placed in coincidence with a 2τ (200-nanosecond) resolution time, chosen short enough to prevent chance coincidences but long enough to compensate for transit-time jitter in the C counter phototube. The $B \cdot C$ signal is fed into an inhibit gate where either an A counter signal, or a readout busy signal, I, inhibits the generation of an $\bar{A} \cdot B \cdot C \cdot \bar{I}$ signal to trigger the high-voltage pulser and initiate the readout electronics.

The B and C counters were calibrated on ground-level cosmic muons; when placed in coincidence they provide excellent separation of signal from noise for relativistic singly charged particles. To test the anticoincidence dome efficiency, a small concidence telescope with a relatively narrow opening angle was placed inside the dome. Cosmic-ray muons were then analyzed to determine if any charged particles were detected by the telescope after not being recorded by the dome. It was found that less than one count in 10^4 escaped detection by the dome.

6. The High-Voltage Pulser

Every two modules of the detector are driven by an Eggerton, Germeschausen, and Grier KN-2 Krytron driven by an avalanche transistor circuit common to eight Krytrons, as shown in Figure 3.15. Each module has its own discharge capacitor to minimize energy robbing between modules. The 2N2087 avalanche transistors provide a fast 800-volt trigger pulse to the grid of each Krytron. A 300-volt converter supplies both the avalanche circuit and a 150-microampere

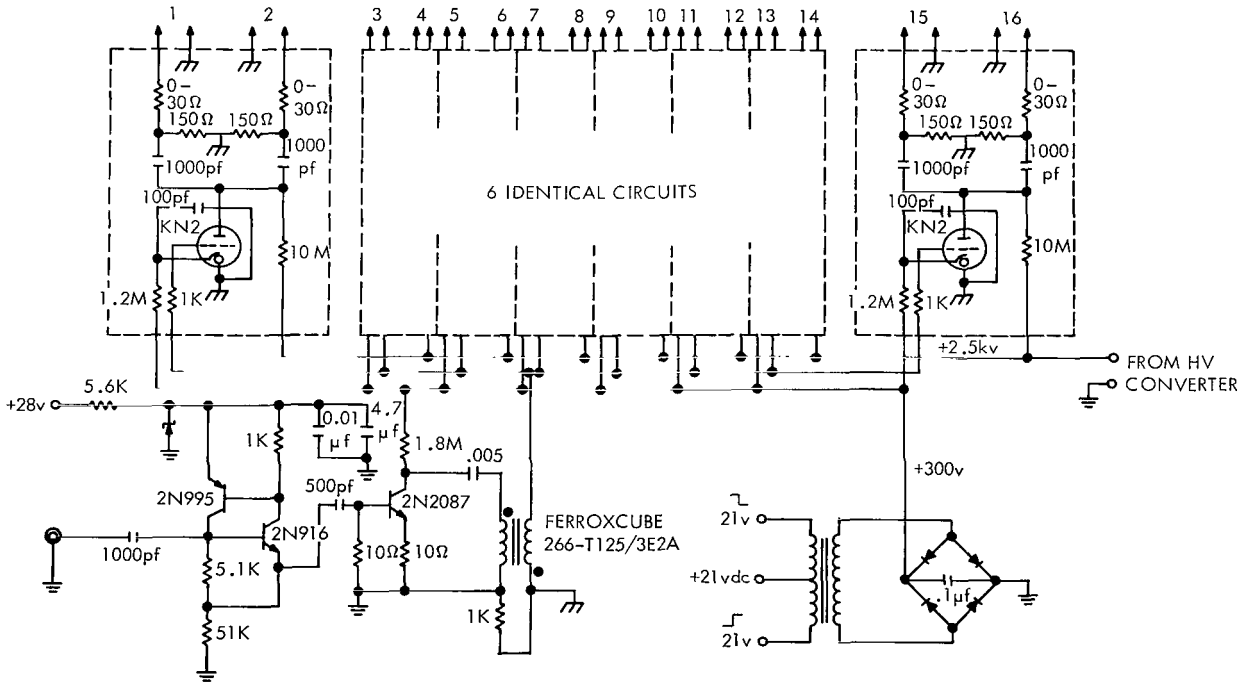

Figure 3.15—Spark-chamber pulser circuit schematic.

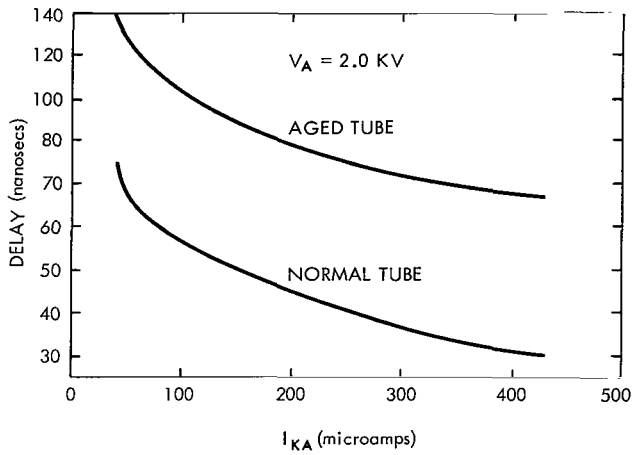

Figure 3.16—Krytron pulser delay as a function of keep-alive current.

Table 3.4

Delays in Triggering the Spark Chamber.

Circuit	Delay (nanoseconds)
Phototube	125
Coincidence circuit	75
Krytron pulser	50
Spark formation	50
Total	300

keep-alive current for each KN-2. This current reduces the delay time between the application of the coincidence trigger and firing of the Krytron on about 50 nanoseconds (Figure 3.16) with a rise time on the plate of about 15 nanoseconds. The total delay from the time of charged-particle passage to the formation of the spark is about 300 nanoseconds, as detailed in Table 3.4. To minimize interaction between the high-voltage pulser circuits and low-signal-level circuits, the grounds are separated by 1 kilohm. In addition, all high-current grounds use large-diameter bus wire to main low inductance. This application of the spark chamber needs no clearing field. The mean time between charged-particle passages through the detector is about a millisecond at balloon altitudes. On this time scale, recombination and impurity attachment suffice to clear out the residual ions. The detector system contains two pulsers of the type shown in Figure 3.15. Each is hermetically sealed, with its self-contained high-voltage power supplies, in a pressure-tight box pressurized with dry nitrogen; this prevents high-voltage breakdown and corona within the pulser circuits. Again, the inputs require only low-voltage power and the low-level coincidence trigger pulse.

7. Flight Gondola and Orientation System

The scientific balloon provides a cheap way to carry detector payloads of a few hundred pounds above 99 percent of the terrestrial atmosphere. Though the secondary photons produced by cosmic-ray interactions in the atmosphere are important even at these altitudes, they are insignificant in a point-source search as will be shown in Chapter V.

For flight, the detector is placed in a gondola that provides orientation with respect to the geomagnetic field. Figure 3.17 shows the detector installed in a gondola equipped for flight. The opposite end of the gondola contains an electronics box that houses batteries, the flight tape recorder, that portion of the electronics not required near the detector, and the electronics associated with the orientation control system. For flight, the gondola is suspended from the balloon load line through a low-friction swivel above its center of mass.

The one-axis orientation system consists basically of two reaction-control jets, supported on booms from either end of the gondola, which receive their error signal from a Schonstedt MND-5C-25

fluxgate magnetometer. Figure 3.18 is a block diagram of the system. After being amplified, the magnetometer signal is summed with a rate loop signal whose output is proportional to the rate of change of position of the rotating gondola. This combined rate plus position signal then activates the switching amplifier, which in turn energizes the reaction control jets if a pointing error greater than about a half degree is presented. The rate loop, consisting of a rate gyro, a demodulator, and a dc amplifier, provides critical damping in the orientation correction.

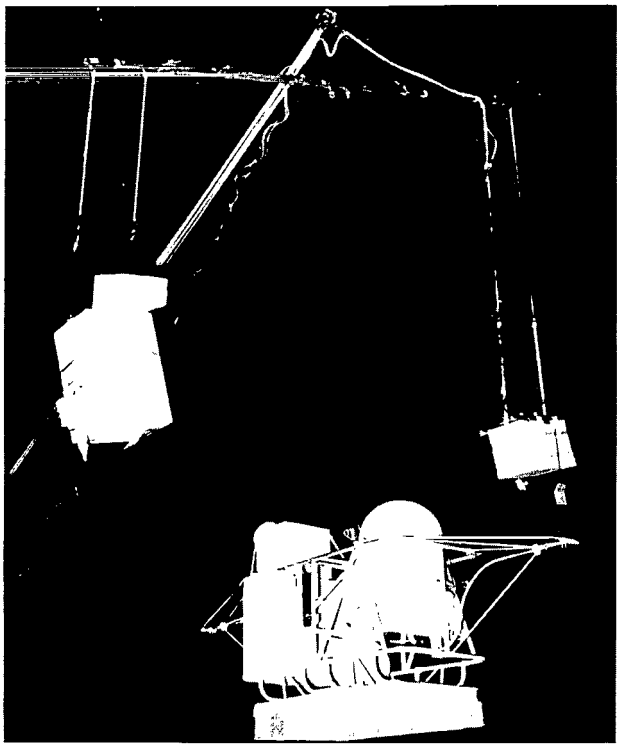

Figure 3.17—The spark chamber installed in its orientation gondola before balloon flight launch.

Should the orientation duty cycle become too high, causing excessive use of gas, the variable-deadband loop is activated; this reduces the gain of the magnetometer output, effectively increasing the maximum acceptable error signal. Thus the duty cycle is reduced until the disturbance causing the increase is removed. Since the orientation error is known from the recorded magnetometer output, this does not destroy orientation information, but does significantly reduce the rate of gas consumption of excessive gas usage caused by turbulence in the atmosphere during ascent of the balloon, the orientation is not turned on until the balloon reaches ceiling.

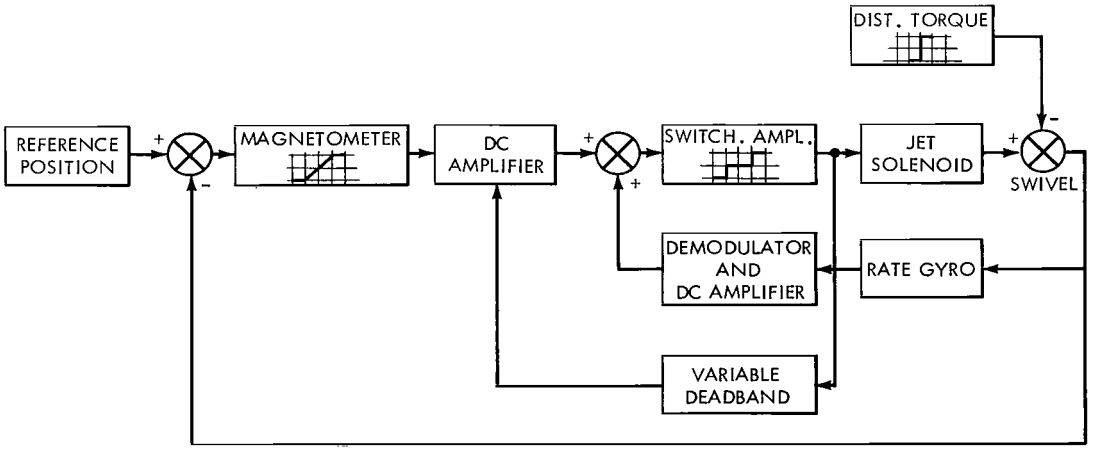

CONTROL SYSTEM BLOCK DIAGRAM

Figure 3.18—Block diagram of the orientation control system.

The weight of the entire gondola prepared for flight is about 350 pounds with an inertia of about 12 slug-feet about the orientation axis. It is found that 0.2 pound of thrust with a 5-foot lever arm allows initial acquisition in about 2 minutes. With the gas-saving features mentioned above, 0.5 cubic feet of nitrogen at 3000 psi at 273°K is more than enough to maintain orientation for a 10- to 12-hour balloon flight. The gas is stored in a 12-inch-diameter spherical bottle mounted beneath the gondola. From the bottle the gas passes through a regulator, where the pressure is reduced to 130 psi, and then passes directly to the solenoid valves that control gas passage through the jets.

Because of the temperature extremes encountered in a balloon flight, the entire detector and orientation system must be built to operate over a wide temperature range. To accomplish this, all electronic systems were designed and tested to operate between -20°C and +50°C. However, certain mechanical tolerances within the structure of the spark chamber itself do not allow the expansion and contraction that would result from such a wide temperature range. Therefore, thermostatically controlled electrical heaters were installed within the spark chamber, and all parts of the system were insulated with styrofoam. Testing of this entire system within an environmental chamber showed that all components of the system were operational over a typical balloon-flight time-temperature profile.

CHAPTER IV

DATA ANALYSIS TECHNIQUES

1. Event Analysis

The first step in the data reduction was the analysis of individual events of the type shown in Figure 3.13. The data were reduced by both hand and computer analysis since this was the first of a series of balloon and satellite flights. Eventually the entire analysis will be handled by computers, with full use of the digital data format.

Initially, each recorded spark event was printed out (Figure 3.13) with separate views of the two orthogonal planes as well as the 45-degree grid information, giving a three-dimensional view of each event. The manual analysis was performed directly on these displays. The type and quality of each event were studied in detail. Both clear pair-production events and other possible events were selected for further analysis. The latter type of events could be either unresolved pairs or some kind of single neutral-induced track. Most of the unacceptable events are tracks coming from the side walls of the spark chamber—presumably caused by secondaries arising from the interactions of neutral particles with the matter of the support structure and accessory equipment in the spark-chamber walls. The top grid was used as an additional anticoincidence device, to eliminate from analysis, in particular, those pairs that were produced in the hemispherical dome of the stainless-steel cover. Any remaining events were retained for further analysis.

Measurements were made on each retained event to determine the arrival direction and opening angle of the electron pair and the multiple scattering of each electron. The chamber arrival direction was then folded together with the time, aspect, and location information to give a celestial arrival direction for the incoming gamma-ray, assuming that it came from outside the atmosphere. The method of obtaining the arrival direction and the analysis of the opening angle and multiple scattering data will be discussed in Sections 2, 3, and 4.

The data were processed automatically by machine, except that at one point a human interface was used to confirm the accuracy of the computerized gamma-ray analysis and, if necessary, reject an obviously erroneous event. The events were automatically examined, categorized and, if accepted, fitted by the least-squares method to a photon trajectory in chamber coordinates; aspect, position, and time data were then automatically used to determine the celestial arrival direction of each photon, and sky maps of the photon flux were constructed, all within the same program. Figure 4.1 shows two examples of (a) the digital display of an event as it comes directly from the data tape, (b) the display of an event after a process is applied to reduce apparent spark spreading and eliminate completely spurious sparks, and (c) a display of the fitted trajectory in the top half of the chambers.

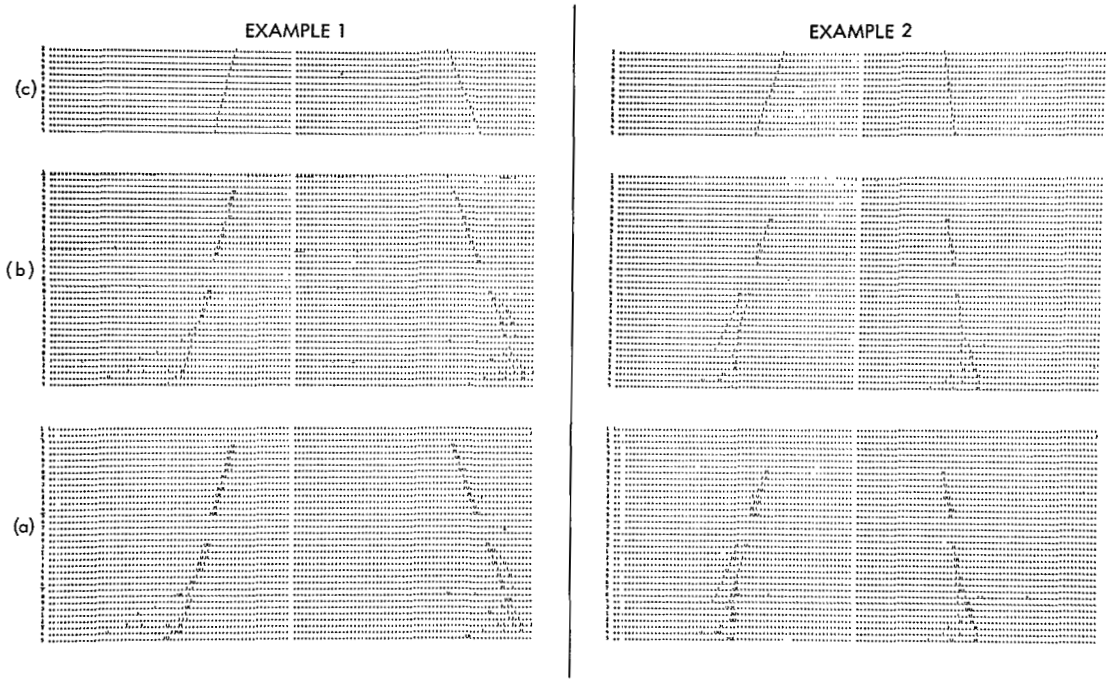

Figure 4.1—Two examples of a digital display of an event (a) as it comes from the data tape, (b) after a process is applied to reduce apparent spark spreading and to eliminate spurious sparks, and (c) a display of the fitted trajectory in the top half of the chamber.

The event analysis program consists of a search moving downward through the chamber for a fit either to an inverted V or to a line segment at the beginning of a spark pattern. It rejects automatically those events that give sparks in the top grid, those that enter through the chamber wall, and those that have too few sparks to treat reliably in the beginning of the pattern or throughout the entire pattern. Comparison with the manual analysis of the several hundred accepted events shows the program reliability to be better than 99 percent for retaining good events, although some of the retained events had to be discarded manually. The random occurrence of spurious sparks and the existence of a complete spectrum of neutral induced events makes an ideal analysis program, approachable only asymptotically. The uncertainty of photon identification therefore increases as the observed pair-production event appears less like an inverted V—as may be the case for low-energy gammas where the electrons scatter profusely after pair formation.

The pair-production events obtained as described above were used to obtain both point-source and atmospheric-background fluxes and to obtain the background energy spectrum. The next three sections will describe the basic measurements used in extracting the required information from the observed events, with the results presented in Chapter V.

2. Energy Estimate Based on Opening Angle

The study of the opening angles of the created electron-positron pair provide two basic pieces of information. First, the bisector of the angle formed by the pair gives the best estimate of the

arrival direction of the gamma-ray. Section 4 will discuss this problem in detail. Second, the opening angle gives an estimate of the energy of the incoming gamma-ray. This problem has been discussed by Olsen (1963); only the applicable results will be considered here. Olsen has considered the kinematics of the three-body decay involving the electron pair and the recoil nucleus. Because of the three particles, the relation between opening angle and gamma-ray energy is not unique, but the most probable relation is given by

$$E_\gamma\,(\text{Mev}) = \frac{1.6}{\theta}, \tag{4.1}$$

where θ is the measured opening angle in radians and E_γ the estimated photon energy in Mev.

This result accounts only for the kinematics of the interaction, whereas for the spark-chamber application the pair opening angle is dominated by the multiple-coulomb interactions of the electron and positron following this formation. Olsen (1963) considers this problem also; and the effects combine to give an energy estimate

$$E_\gamma = 2a\left[1 + \left(\ell n\, 2a^2 + 1.29\right)/4a^2\right]/\theta\,, \tag{4.2}$$

where $a^2/2$ is the mean-square lateral deflection of one electron. The scattering calculations of Pinkau (1966) for a multiplate chamber show that for relativistic single charged particles

$$a^2 \approx \frac{412 B_d\, \delta_{n_p}}{X_0\left[\ell n\left(183 Z_s^{-1/3}\right)\right] n_p \Delta^2}, \tag{4.3}$$

$$\delta_{n_p} = \left[\frac{d}{4}\left(\Delta^2 + \frac{d^2}{3}\right) + \left(\frac{n_p^2 - 1}{3}\right)\Delta^2 d\right] \tag{4.4}$$

$$\frac{1}{B_d}\, e^{B_d} = 6.68 \times 10^3\, \rho_s\, dC \tag{4.5}$$

$$C = \frac{\left(Z_s + 1\right) Z_s^{1/3}}{A_s\left(1 + 3.34\, \alpha_s^2\right)} \tag{4.6}$$

where

X_0 = radiation of the scattering material

Z_s = atomic number of the scattering material

α_s = $Z_s/137$ (for relativistic electrons)

ρ_s = density of scattering material (g cm^{-3})

d = thickness of scattering plate (cm)

Δ = 2a + d

2a = distance separating the plates (cm)

n_p = number of plates through which the particle has passed

A_s = atomic weight of the scattering material.

Olsen also found the confidence limit in obtaining the energy, using Equation 4.2:

$$C\left(\frac{\Delta E_\gamma}{E_\gamma}\right) \approx \frac{\Delta E_\gamma}{E_\gamma} . \tag{4.7}$$

Hence the error in the energy estimate is quite large—about one part in two for 50-percent confidence. For this reason, below 500 Mev, where the scattering signal becomes measurable, the electron scattering technique provides a more trustworthy estimate of photon energy.

3. Multiple Coulomb Scattering in the Multiplate Spark Chamber

The theory of multiple Coulomb scattering has been worked out in great detail by Williams (1939) and Moliere (1947, 1948, and 1955) and by many others (Goudsmit and Saunderson, 1940; Snyder and Scott, 1949; Scott, 1952; and Bethe, 1953) and used successfully for many years an in energy-determination technique in the study of fast charged particles in nuclear emulsions (Fowler, 1950; and Voyvodic and Pickup, 1952) and cloud chambers (Olbert, 1952; and Annis, Bridge, and Olbert, 1953). More recently the method has been applied to multiplate spark chambers by Pinkau (1966 and 1967). Closely following the Moliere theory, Pinkau has shown that the distribution function for multiple scattering through a thickness z cm of a given material is given by

$$f(z, \phi, x) = \frac{1}{(2\pi)^2} \int_{-\infty}^{\infty}\int d\eta_1 \, d\eta_2 F(z, \eta_1, \eta_2) \, e^{i\phi\eta_1 + i\chi\eta_2} , \tag{4.8}$$

where the coordinates are those shown in Figure 4.2. This distribution function applies to the scattering coordinates projected onto a plane containing the x-axis. The Fourier transform $F(z, \eta_1, \eta_2)$ is given by Moliere (1947, 1948, and 1955) and for relativistic electrons may be expressed by

$$F(z, \eta_1, \eta_2) = \exp\left\{-\frac{J_z^2 z}{4}\left(\eta_1^2 + \eta_1\eta_2 z + \eta_2^2 \frac{z^2}{8}\right) + \frac{J_z^2}{12B_2}\left[\frac{(\eta_1 + 2\eta_2)^3}{\eta^2} \ln \frac{J_z^2 z(\eta_1 + 2\eta_2)^2}{4e^{2/3}} - \frac{\eta_1^3}{\eta_2} \ln \frac{J_z^2 z(\eta_1^2)}{4e^{2/3}}\right]\right\} , \tag{4.9}$$

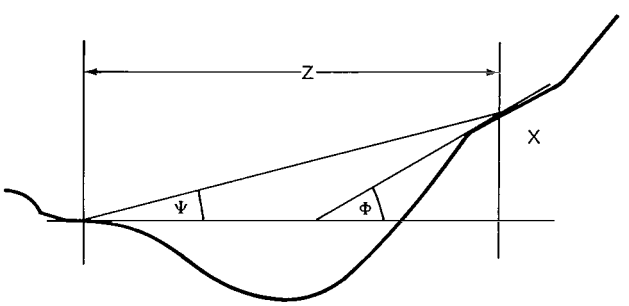

Figure 4.2—Coordinates used in the scattering distribution function.

where

$$J_z^2 = \chi_c^2 B_z$$

$$\chi_c^2 = \frac{4\pi N_s e^4 Z_s (Z_s + 1)}{(p_e v_e)^2} \tag{4.10}$$

N = density of atoms in the scattering material

$$\frac{e^{B_z}}{B_z} = \frac{\chi_c^2 z}{\chi_a^2}$$

ρ_s = density of the scattering material.

χ_a is the screening angle from the Moliere theory. This single parameter describes the scattering, while the ratio $\chi_c z/\chi_a$ describes the angular distribution due to scattering in a material thickness z. The assumptions concerning the specific shape of the differential cross section are contained in χ_a. Using a Thomas-Fermi potential and the WKB method, Moliere obtains

$$\chi_a = \left(\frac{\bar{\lambda}}{a}\right)^2 \left(1.32 + 4.39\,\alpha^2\right), \tag{4.11}$$

where $\bar{\lambda}$ is the de Broglie wavelength of the electron, and a_f is the Fermi radius of the atom. α^2 expresses the deviation from the Born approximation. Inserting the appropriate values for these parameters gives

$$\frac{1}{B_z} e^{B_z} = \frac{6680\, z\left(Z_s + 1\right) Z_s^{1/3}}{A_s\left(1 + 0.00018\, Z_s^2\right)} \tag{4.12}$$

for relativistic electrons.

To apply these results to measurements that can be made in the digitized spark chamber discussed in Chapter III, we use the method of constant cell size described by Fowler (1950) for nuclear emulsions and applied to the spark chamber by Pinkau (1966 and 1967). The appropriate quantity to be measured is $\beta = x - 2x' + x''$, where x, x', and x'' are the projected coordinates in Figure 4.3. Generalizing Pinkau's results to readings taken every n_pth plate gives the probability for obtaining successive readings of x, x', and x'', for arbitrary angles ϕ, ϕ', and ϕ'', as

$$W_{n_p}(x, x', x'') = \int_{-\infty}^{\infty}\iint d\phi\, d\phi'\, d\phi''\, n_p\, \Delta f\left(n_p\Delta, \phi - \phi', x - x' - n_p\Delta\phi'\right) \cdot f\left(n_p\Delta, \phi' - \phi'', x' - x'' - n_p\Delta\phi''\right). \tag{4.13}$$

Pinkau shows that

$$F\left(n_p\Delta, \eta_1, \eta_2\right) = \exp\left[-\frac{J_d^2}{4}\left(u_{n_p}\eta_1^2 + v_{n_p}\eta_1\eta_2 + \omega_{n_p}\eta_2^2\right)\right], \tag{4.14}$$

where

$$u_{n_p} = nd$$

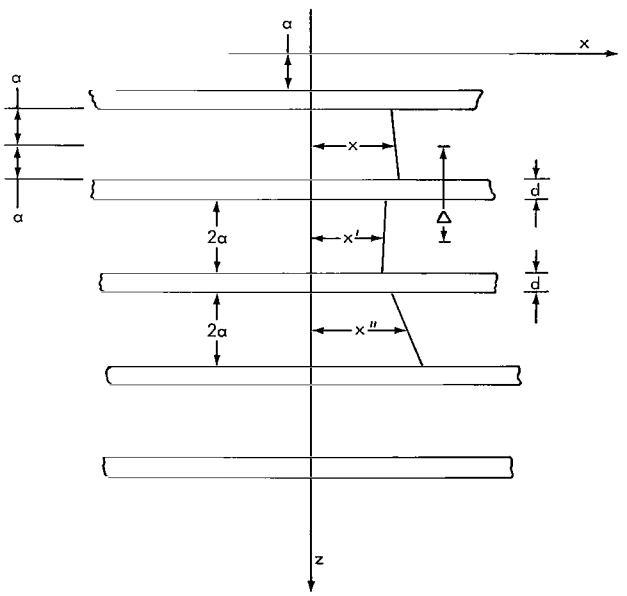

Figure 4.3—Scattering coordinates in the spark chamber.

$$v_{n_p} = n_p^2 \Delta d$$

$$\omega_{n_p} = n_p \frac{d}{4}\left(\Delta^2 + \frac{d^2}{3}\right) + \frac{(n_p + 1)\, n_p (n_p - 1)}{3} \Delta^2 d \, .$$

Only the gaussian part of Equation 4.9 has been retained here, introducing an error of 10 percent or less in the final results. Using Equation 4.8 to obtain

$$f\left(n_p \Delta, \phi - \phi', x - x' - n_p \Delta\phi'\right)$$

and

$$f\left(n_p \Delta, \phi' - \phi'', x' - x'' - n_p \Delta\phi''\right) ,$$

substituting in Equation 4.13, and making use of the relation

$$\int_{-\infty}^{\infty} e^{i\alpha x}\, d\alpha = 2\pi\delta(x) ,$$

gives

$$W_{n_p}(x, x', x'') = \frac{1}{2\pi n_p \Delta} \int_{-\infty}^{\infty} d\eta' \, F\left(n_p \Delta, 0, \frac{\eta'}{n_p \Delta}\right)$$

$$\cdot \, F\left(n_p \Delta, \eta', -\frac{\eta'}{n_p \Delta}\right) \exp\left[i\eta' \frac{x - 2x' + x''}{n_p \Delta}\right]$$

or

$$W_{n_p}\left(\beta_{n_p}\right) = \frac{1}{2\pi} \int_{-\infty}^{\infty} d\eta e^{i\eta\beta} F\left(n_p \Delta, 0, \eta\right) F\left(n_p \Delta, \eta n_p \Delta, -\eta\right) . \qquad (4.15)$$

Equation 4.14 gives

$$F\left(n_p \Delta, 0, \eta\right) = \exp\left[-\frac{J_d^2}{4} \omega_{n_p} \eta^2\right]$$

$$F(n_p \Delta, n_p \Delta\eta, -\eta) = \exp\left[-\frac{J_d^2}{4}\left(u_{n_p} n^2 \Delta^2 - v_{n_p} n_p \Delta + \omega_{n_p}\right)\eta^2\right]$$

$$= \exp\left[-\frac{J_d^2}{4}\omega_{n_p}\eta^2\right],$$

and therefore

$$W_{n_p}(\beta_{n_p}) = \frac{1}{2\pi}\int_{-\infty}^{\infty} d\eta e^{i\eta\beta} \exp\left[-\frac{J_d^2}{4}\left(2\omega_{n_p}\right)\eta^2\right]$$

$$= \frac{1}{2\pi}\int_{-\infty}^{\infty} d\eta e^{i\eta\beta} \exp\left[-\frac{\left(J_d Q_{n_p}\eta\right)^2}{4}\right], \qquad (4.16)$$

where

$$Q_{n_p} = \sqrt{2\omega_{n_p}}.$$

Integrating Equation 4.16 gives

$$W_{n_p}(\beta_{n_p}) = \frac{2}{J_d Q_{n_p}\sqrt{\pi}} e^{-\beta_{n_p}^2 / J_d^2 Q_{n_p}^2},$$

where we note that the normalization is

$$\int_0^{\infty} W_{n_p}(\beta_{n_p})\, d\beta_{n_p} = 1.$$

Thus the mean of the absolute value of $|\beta_{n_p}|$ is

$$\langle|\beta_{n_p}|\rangle = \int_0^{\infty} \beta_{n_p} W_{n_p}(\beta_{n_p})\, d\beta_{n_p}$$

$$= \frac{2}{J_d Q_{n_p}\sqrt{\pi}} \int_0^{\infty} \beta_n e^{-\beta_n^2 / J_d^2 Q_{n_p}^2}\, d\beta_{n_p}$$

$$= \frac{J_d Q_{n_p}}{\sqrt{\pi}}. \qquad (4.17)$$

For the spark chamber used in this experiment, the appropriate parameters are

$d = .0064$ cm

$a = 0.37$ cm

$Z_s = 79$

$A_s = 197$

$X_0 = 6.00$ g cm^{-2}.

Using Equations 4.12 and 4.10, we obtain

$$J_d = \frac{28.9}{(p_e v_e)}.$$

Since, for relativistic electrons $pv \approx E_e$, this gives (using Equation 4.17)

$$\langle|\beta_{n_p}|\rangle E_e = 16.3 Q_{n_p} \text{ Mev cm}. \tag{4.18}$$

Up to this point we have considered the scattering signal as consisting of contributions from Coulomb scattering alone. In practice this is not the case; there is a random noise signal (mostly reading noise and random fluctuations of the spark from the track location) that must be considered. Since both the scattering signal which we have considered and noise are gaussian-distributed, they add as

$$\langle|\beta_1|\rangle^2 = \langle|\beta_s|\rangle^2 + \langle|n_0|\rangle^2,$$

where β_s is the Coulomb scattering signal for one plate and n the noise contribution for scattering in a single plate. It follows that

$$\langle|\beta_2|\rangle^2 = \frac{Q_2^2}{Q_1^2}\langle|\beta_s|\rangle^2 + \langle|n_0|\rangle^2 \tag{4.19a}$$

$$\langle|\beta_{n_p}|\rangle^2 = \frac{Q_{n_p}^2}{Q_1^2}\langle|\beta_s|\rangle^2 + \langle|n_0|\rangle^2. \tag{4.19b}$$

In this manner we may eliminate $\langle|n_0|\rangle$ and obtain, for instance,

$$\langle|\beta_s|\rangle_{21} = Q_1\left[\frac{\langle|\beta_2|\rangle^2 - \langle|\beta_1|\rangle^2}{Q_2^2 - Q_1^2}\right]^{1/2} \tag{4.20}$$

and therefore

$$(E_e)_{21} = 14.3 \left[\frac{Q_2^2 - Q_1^2}{\langle|\beta_2|\rangle^2 - \langle|\beta_1|\rangle^2} \right]^{1/2} , \tag{4.21}$$

where the noise contribution has been eliminated. To obtain a final energy for the electron, correct the measured energy for bremstrahlung radiation losses from the point of pair formation to the point of energy measurement.

Using Equation 4.19 we can also obtain the noise contribution which gives, for instance,

$$\langle|n_0|\rangle^2 = \frac{Q_1^2 \langle|\beta_2|\rangle^2 - Q_2^2 \langle|\beta_1\rangle^2}{Q_1^2 - Q_2^2} . \tag{4.22}$$

4. Determination of Gamma-Ray Arrival Direction

To find the arrival direction of the gamma-ray it is first necessary to find a direction for each electron of the formed pair. When the energy of an accepted gamma-ray has been obtained, a determination is made of the number of scattering plates, n, through which the electrons must pass before the scattering signal becomes of the same order of magnitude as the combined measurement errors. Then a least-squares fit is made to each electron through the n plates, beginning at the apex of the pair formation. Making the measurement over this distance provides maximum information on track location with minimum possible error in the data. With the projected direction of each electron determined in each of two orthogonal planes, the projected angles of the bisector, ϕ_x and ϕ_y, are used to estimate the photon arrival direction.

To estimate the gamma-ray arrival direction by the pair bisector introduces an error due to the random statistical nature of electron scattering. To find the error magnitude, it is again necessary to consider the electron scattering. The distribution function for electron lateral displacement due to multiple scattering after passing through n plates is (Pinkau, 1966)

$$f(n_p \Delta, y) = \frac{1}{J_d \sqrt{\pi \omega_{n_p}}} e^{-y^2 / J_d^2 \omega_{n_p}} , \tag{4.23}$$

where the parameters are defined in Section 3. This distribution function is used to obtain the probability, for all possible scattering paths of the two electrons, that the pair bisector falls within some preselected cone of angular uncertainty about the gamma-ray arrival direction. The error in the arrival direction is taken as the angular square within which 95 percent of the bisectors are expected to fall; the error is an inverse function of energy, as shown in Figure 4.4.

To obtain the extrapolated celestial arrival direction, take the chamber coordinates ϕ_x and ϕ_y and convert them to celestial right ascension and declination (Figure 4.5). Here λ is the latitude of the balloon location, N the North geographic pole, V the vertical vector of the balloon location,

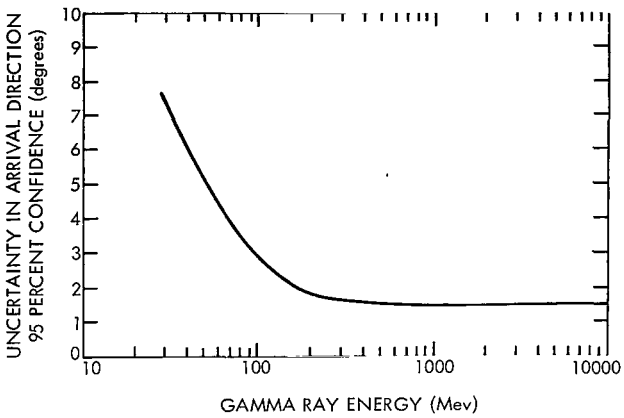

Figure 4.4—The 95-percent confidence limit uncertainty in the arrival direction (incurred by approximating the gamma-ray arrival direction by the bisector of the formed electron-positron pair) plotted as a function of gamma-ray energy.

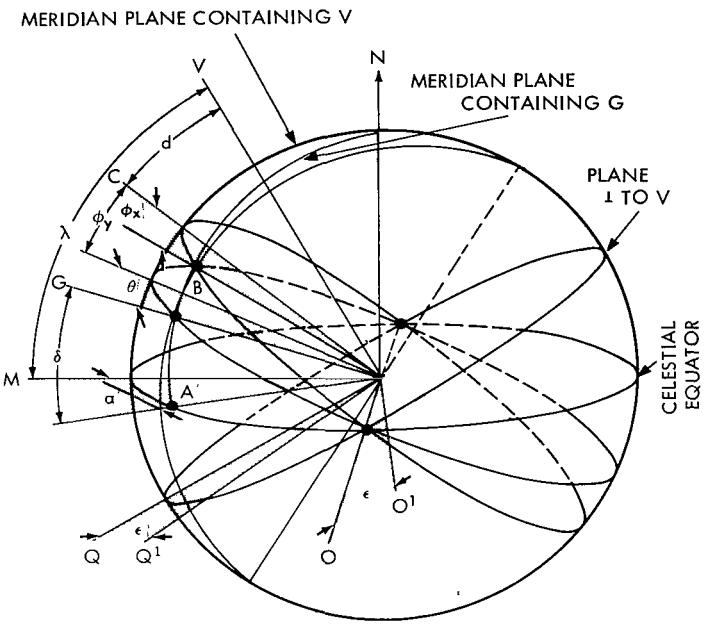

Figure 4.5—Transformation of chamber coordinates (ϕ_x, ϕ_y) to celestial coordinates (α, δ) (remaining coordinates are described in the text).

M the intersection of the meridian plane containing the V vector with the equatorial plane, α the hour angle of the observed gamma-ray direction G, C the pointing direction of the chamber ($\phi_x = \phi_y = 0$), which lies on angle d below V in the meridian plane, and δ the declination of the observed gamma-ray. Then

$$G_N = G \cos\theta \sin(\lambda - \phi_y - d) \tag{4.24}$$

$$G_M = G \cos\theta \cos(\lambda - \phi_y - d)$$

$$G_0 = G \sin\theta \,. \tag{4.25}$$

Thus

$$\tan\alpha = \frac{G_0}{G_M} = \frac{\tan\theta}{\cos(\lambda - \phi_y - d)}$$

and

$$\sin\delta = \frac{G_N}{G} = \cos\theta \sin(\lambda - \phi_y - d) \,.$$

Since

$$\tan\phi_x = \frac{G \sin\theta}{G \cos\theta \cos\phi_y} = \frac{\tan\theta}{\cos\phi_y} \,,$$

then

$$\tan\alpha = \frac{\tan\phi_x \cos\phi_y}{\cos(\lambda - \phi_y - d)} \tag{4.26}$$

$$\sin\delta = \cos\left[\tan^{-1}\left(\tan\phi_x \cos\phi_y\right)\right] \sin(\lambda - \phi_y - d) \ . \tag{4.27}$$

On a celestial sky map of the observed gamma-rays (assuming that they come from outside the atmosphere) the right ascension is

$$\alpha_{R.A.} = GMS_{id}\, T_0 + 1.00274 \times \text{Time} - \text{West Longitude} + \alpha \text{ (hours)} \ , \tag{4.28}$$

where times are measured in hours and $GMS_{id}\ T_0$ = Greenwich Mean Sidereal Time at 0 hrs. U.T.

Equations 4.26 and 4.27 are based on the assumption that the orientation system maintains the detector axis in the meridian plane throughout the flight. However, in practice, small errors in rotation might be introduced causing a rotation of the gondola about the vertical axis by an angular interval ϵ. Such errors may be introduced by longitude variations in the deviation of the magnetic field over the duration of the balloon flight, by torquing of the balloon load lines in a constant direction, and by other minor malfunctions of the orientation system. The longitude variations of the terrestrial magnetic field are normally negligible; however, torquing of the balloon load line may introduce an error of up to 2 degrees rotation about the vertical. Such a rotation is detectable by the output signal of the orientation magnetometer and may be used to determine the magnitude and sense of the rotation.

Referring again to Figure 4.5, for a rotation about V such that O becomes O′ and Q becomes Q′, the projections of G onto N, M and O become

$$\begin{aligned}
G_N &= G\cos\theta\cos\left(d+\phi_y\right)\sin\lambda + G\sin\theta\sin\epsilon\cos\lambda \\
&\quad - G\cos\theta\sin\left(d+\phi_y\right)\cos\epsilon\cos\lambda \\
G_M &= G\cos\theta\sin\left(d+\phi_y\right)\cos\epsilon\sin\lambda - G\sin\theta\sin\epsilon\sin\lambda \\
&\quad + G\cos\theta\cos\left(d+\phi_y\right)\cos\lambda \\
G_0 &= G\sin\theta\cos\epsilon + G\cos\theta\sin\left(\phi_y+d\right)\sin\epsilon \ .
\end{aligned} \tag{4.29}$$

Using the approximation that $\sin \epsilon \approx \phi$ and $\cos \epsilon \approx 1$ leads to the equivalents of Equations 4.26 and 4.27:

$$\tan \alpha = \frac{\tan \phi_x \cos \phi_y + \epsilon \sin(d + \phi_y)}{\cos(\lambda - \phi_y - d) - \epsilon \tan \phi_x \cos \phi_y \sin \lambda} \tag{4.30}$$

$$\sin \delta = \cos \left[\tan^{-1}(\tan \phi_x \cos \phi_y)\right] \sin(\lambda - \phi_y - d) - \epsilon \sin \left[\tan^{-1}(\tan \phi_x \cos \phi_y)\right] \cos \lambda . \tag{4.31}$$

Equations 4.30 and 4.31 reduce to Equations 4.26 and 4.27 for $\epsilon = 0$. Equation 4.28 then gives the right ascension, and Equation 4.31, gives the declination.

5. Detection Efficiency as a Function of Energy

In order to determine the absolute value of the flux or flux upper limit represented by the observations, it is necessary to know the efficiency of the detector (a complicated function of the energy and arrival direction of the gamma-ray) and the detector geometry. At high energies the efficiency is a separable function of the pair production efficiency (Figure 4.6), and the effective area exposed to the source (Figure 4.7) is a function of the hour angle relative to the source:

$$\int_{11.83}^{13.60} \text{Area}\, dt = 3.73 \times 10^5 \text{ cm}^2 \text{ sec} .$$

At low energies the efficiency is altered by electron scattering, which causes photons normally falling within the acceptance cone to go

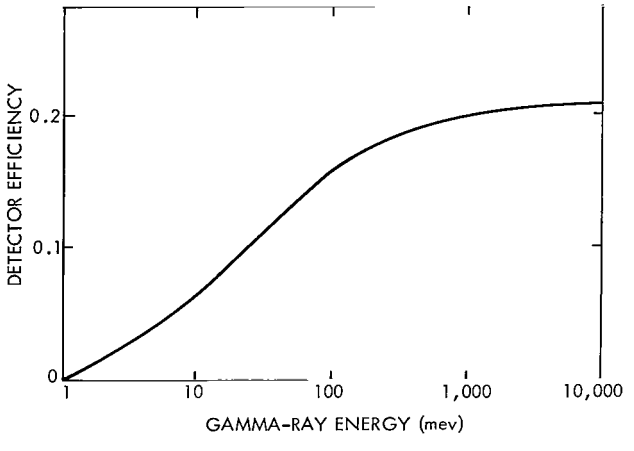

Figure 4.6—Pair production efficiency vs photon energy for the digitized spark chamber used in experiment.

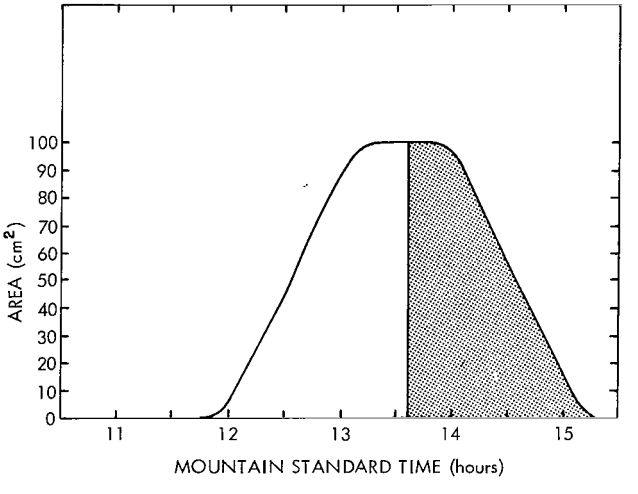

Figure 4.7—Detector area exposed to the Crab nebula as a function of time. Shaded area represents time during which a detector malfunction prevented the acquisition of useful data.

undetected since the electrons scatter out of the coincidence telescope. On the other hand, electrons coming from photons that do not normally fall within the acceptance cone may scatter into the coincidence cone.

To calculate the effect of scattering at low energies, we must again refer to the scattering functions $f(z, \phi, x)$ and $f\left(z + n_p \Delta, \phi - \phi', y - y' - n_p \Delta \phi'\right)$ discussed in Section 3. Assume that on the average each electron passes through 24 of the gold plates prior to reaching the Čerenkov counter at the bottom of the chamber. Then the probability that a particle with a projected angle ϕ' and position x' will have a projected angle ϕ and position x at the Čerenkov counter is given by $f(0, \phi', x')\, f(24\Delta, \phi - \phi', x - x' - 24\Delta\phi')$. Substituting for the functions from Section 3 and integrating over ϕ, we obtain the probability

$$f(24\Delta, x - x' - 24\Delta\phi') = \frac{E_e}{180} \exp \cdot \left[- \left(\frac{E_e}{102} \right)^2 (x - x' - 24\Delta\phi')^2 \right] .$$

Hence, for a given ϕ' and x' at the position of pair formation, the probability that one of the electrons falls between x_1 and x_2 at the Čerenkov counter is given by

$$f(24\Delta) = \frac{E_e}{180} \int_{x_1}^{x_2} \exp \left[- \left(\frac{E_e}{102} \right)^2 (x - x' - 17.8\,\phi')^2 \right] dx$$

$$= \frac{1}{\sqrt{2\pi}} \int_{E/72(x_1 - x' - 17.8\phi')}^{E_e/72(x_2 - x' - 17.8\phi')} e^{-\chi^2/2}\, d\chi . \qquad (4.32)$$

Note that Equation 4.32 is simply the error function, which may be integrated numerically over x' and ϕ' and (in closed form) for x_1 and x_2. The results applied to two electrons—averaged over the typical values of ϕ' for a balloon flight point source exposure and corrected for the pair production efficiencies—are plotted as a function of energy in Figure 4.8. This curve represents the total area-time-efficiency factor and may be combined with the live-time correction to obtain the effective area-time-efficiency factor as a function of energy. Figure 4.9 contains the geometric factor, corrected for pair-production efficiency, for an isotropic gamma-ray intensity, plotted as a function of gamma-ray energy.

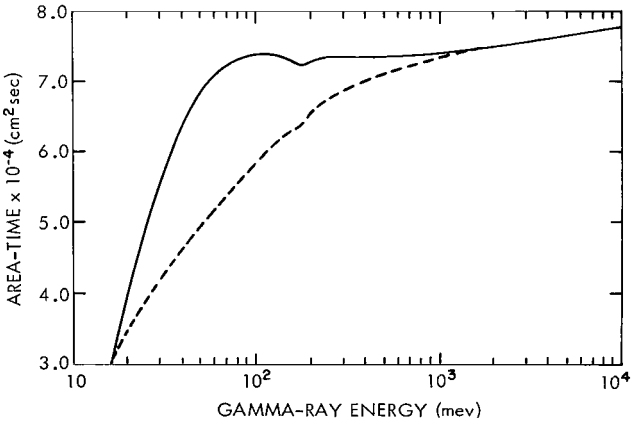

Figure 4.8—Area-time-efficiency factor for point sources plotted as a function of photon energy and including the effects of pair-production efficiency and scattering of the electrons. The dashed curve indicates the results with electron scattering neglected. The dip at about 200 Mev in both curves is probably due to approximations in the calculations rather than a real effect.

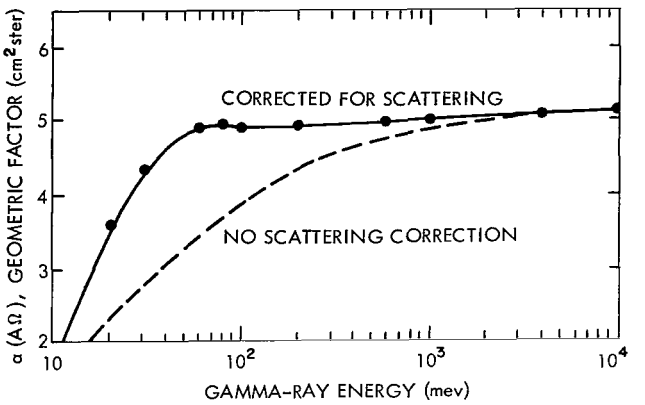

Figure 4.9—Area/solid-angle/efficiency factor for an isotropic intensity plotted as a function of photon energy including scattering effects. The dashed curve represents the results neglecting scattering.

The calculations made in this chapter will now be applied to the data to obtain the intensity and energy spectrum of the background gamma-radiation and obtain the upper limit to the flux of gamma-rays from the Crab nebula.

CHAPTER V

RESULTS

1. Balloon Flight

The data were obtained from a balloon flight launched at 0545 U.T. on September 8, 1966 from Holloman Air Force Base, New Mexico. The balloon reached ceiling at about 1000 U.T. where it floated at about three and a half grams cm^{-2} for 6.5 hours with the $\phi_x = 0$ axis scanning from 2.0 to 8.4 hours in celestial right ascension, providing detector sensitivity from 0.3 to 10.1 hours right ascension and 0 to 48 degrees declination. The area exposed to the Crab nebula as a function of time is given in Figure 4.7. Unfortunately, at 13.6 hours U.T. a malfunction in the detector prevented the acquisition of further gamma-ray data. The shaded portion of Figure 4.7 represents that portion of the area-time curve normally available which was lost because of the malfunction, reducing the normal detector sensitivity by about one-half and restricting the coverage in right ascension.

Table 5.1 summarizes the data related to the balloon flight. The altitude data are only approximate since the photobarograph and baracoder for obtaining pressure data both failed. The altitude data are estimated by radar data, theoretical predictions, and the performance history of this type of balloon. (The error in the estimate has negligible effect on the upper limits to the point source flux.)

Because of the detector malfunction midway through the flight, and a short livetime (about 22 percent), not enough gamma-rays were obtained to give an energy spectrum of atmospheric-produced

Table 5.1

Balloon Flight Data.

Date	September 8, 1966
Launch time	0545 U.T.
Float time	1000 to 1630 U.T.
Trajectory	1000: 32.9° North latitude, 106.8° West longitude
	1630: 32.2° North latitude, 108.6° West longitude
Altitude	Approximately 3.5 grams cm^{-2}
Balloon	10.6×10^6 cubic feet Winzen Stratofilm
Chamber tilt (d in Figure 4.4)	9.0 degrees south of vertical

gamma-rays. Hence, data from a flight made on December 10, 1966, from Mildura, Victoria, Australia, were used for the atmospheric spectrum. For this flight, the average latitude was 33.7°S, and the altitude at float averaged 3.0 grams cm^{-2} with a duration at ceiling of about 2.1×10^4 seconds.

The following sections will analyze the data from these two flights, to obtain the upper limit to the flux of gamma-rays emanating from the Crab nebula and obtain the atmospheric secondary gamma-ray spectrum.

2. Flux Limit for Gamma-Rays from the Crab Nebula

By means of the equations developed in Section 4 of Chapter IV, and the balloon time and position data, each possible gamma-ray was analyzed to determine its arrival direction and the extrapolation of that direction onto the celestial sphere. Figure 5.1 shows the results in celestial

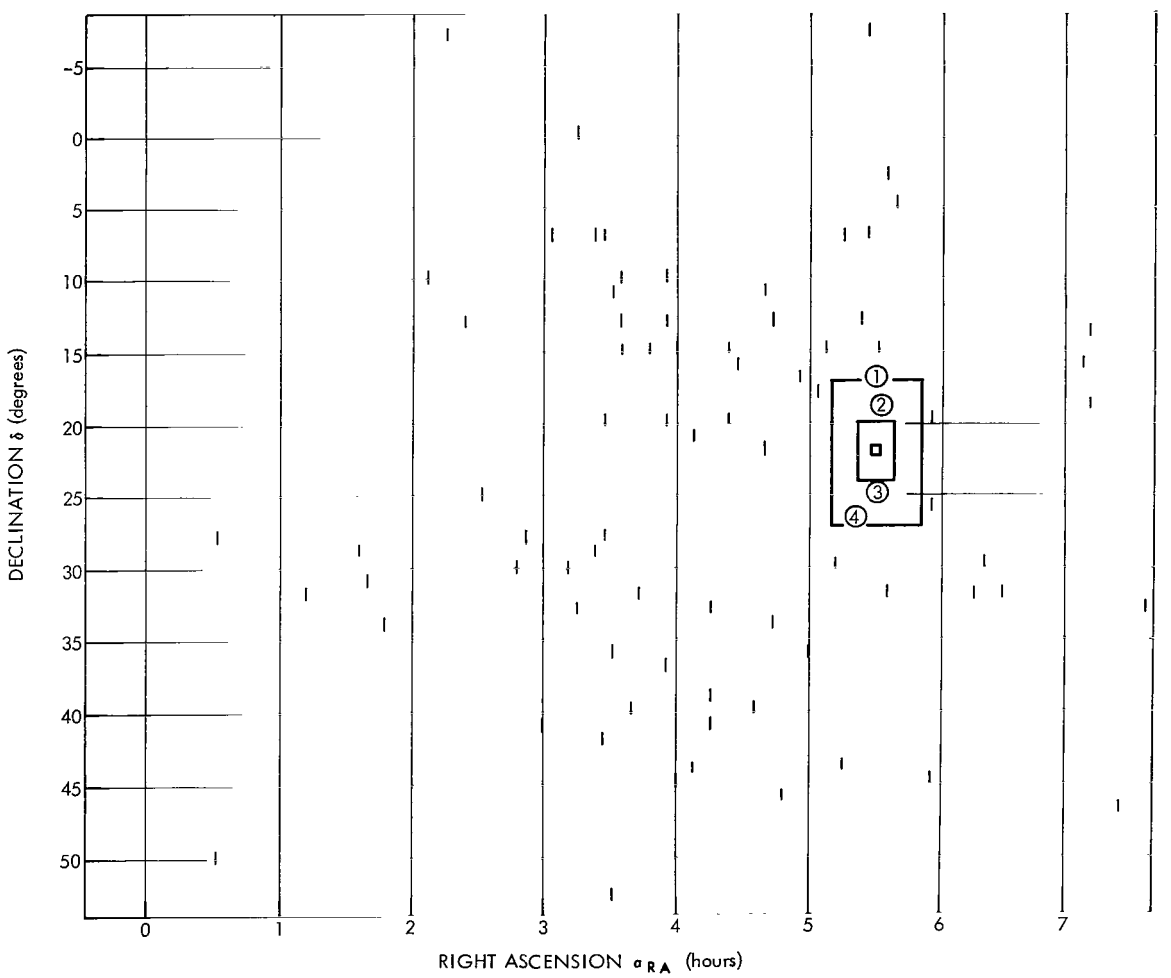

Figure 5.1—Extrapolated celestial coordinates of all observed pairs and possible pairs. The position of the Crab nebula is denoted by a small square. Larger squares are discussed in text.

coordinates. In addition to obvious pairs, these data include "single-track" events, which are any type of single tracks produced by a neutral particle within the chamber. About two thirds of these events appear to be unresolved high-energy ($\geq$500 Mev) pairs. The remainder scatter profusely, indicating low-energy charged particles. The number of such events can be attributed to electrons arising from the Compton scatter of low-energy photons. This process is important only at low energies, as indicated in Figure 3.1. This point will be discussed quantitatively in Section 3, where the atmospheric secondary spectrum is obtained and the statistics can give the number of Compton scatters to be expected.

In Figure 5.1, a small square indicates the position of the Crab nebula. Two enclosing squares, with sides of ±2 degrees and ±5 degrees, respectively, indicate approximately the area of uncertainty in arrival direction for gamma-rays with energies >100 Mev and 30 Mev $\leq E_\gamma \leq$ 100 Mev, respectively. It can be seen that no observed gamma-rays fall within the square of ±2 degrees. Of the tracks numbered 1-4 that fall within the larger square, only track number 3 has an uncertainty in the estimate of its arrival direction that does not allow it to be discarded as shown in Table 5.2.

Figure 5.1 shows that no point sources of gamma-rays were detected. To calculate the flux upper limit, compute the background intensity, as follows: divide all tracks observed (during the duration of the flight, at ceiling) into energy bins of 30 Mev $\leq E_\gamma \leq$100 Mev and E_γ > 100 Mev; the intensity is given by

$$I_{b.g.} = \frac{\text{Number of Gammas Observed}}{\alpha \cdot (A \cdot \Omega) \cdot t \cdot f} , \qquad (5.1)$$

where

α = pair production efficiency,

$A \cdot \Omega$ = solid angle-area factor,

Table 5.2

Details of Pairs Falling Within Uncertainty Cone.

Track	Right Ascension (degrees)	Declination (degrees)	Energy (Mev)	Directional Uncertainty 95 Percent Confidence (degrees)
1	84.9	+17.5	91	3.0
2	85.9	+19.1	37	6.3
3	84.2	+25.9	79	3.4
4	79.9	+27.2	47	5.0
Crab nebula	82.7	+22.1		

t = time at ceiling, and

f = live time factor.

For this detector the parameters are

$$\left[\alpha \cdot (A \cdot \Omega)\right]_{30\text{-}100} \approx 4.6\ \text{cm}^2\,\text{ster}, \quad \left[\alpha \cdot (A \cdot \Omega)\right]_{>100} \approx 4.9\ \text{cm}^2\,\text{ster}.$$

$t = 1.45 \times 10^4$ seconds and $f = 0.22$. The formula for the solid-angle-area factor at asymptotically high energies is developed in Appendix A, and the energy dependence of the geometric-efficiency factor is given in Figure 4.9.

The number of observed pairs in the 30- to 100-Mev and $E_\gamma > 100$ Mev energy ranges are 34 and 28, respectively, giving

$$I_{b.g.}\ (30 \le E_\gamma \le 100) = (2.3 \pm .5) \times 10^{-3}\ \text{cm}^{-2}\,\text{ster}^{-1}\,\text{sec}^{-1} \tag{5.2a}$$

and

$$I_{b.g.}\ (E_\gamma > 100) = (1.8 \pm .5) \times 10^{-3}\ \text{cm}^{-2}\,\text{ster}^{-1}\,\text{sec}^{-1}. \tag{5.2b}$$

These values are in good agreement with the intensities observed by other investigators (Cobb, Duthie, and Stewart, 1965; Frye and Smith, 1966; and Fazio, *et al.*, 1967). To obtain the expected number of secondary or background gamma-rays for the squares of ±5 degrees and ±2 degrees, we first note that the solid angle for these squares is approximately $(10/57.3)^2$ and $(4/57.3)^2$ steradians, respectively. The time-area-efficiency factor given in Figure 4.8 gives the expected number in the uncertainty squares as

$$N_{b.g.}\ (30 \le E_\gamma \le 100) = (2.3 \times 10^{-3}) \left(\frac{10}{57.3}\right)^2 (7.08 \times 10^4)\ (0.22)$$

$$= 1.09$$

$$N_{b.g.}\ (E_\gamma > 100) = (1.8 \times 10^{-3}) \left(\frac{4}{57.3}\right)^2 (7.35 \times 10^4)\ (0.22)$$

$$= 0.14.$$

Poisson statistics give the flux limits as follows: we must find a flux limit that the actual flux has less than a 5-percent chance of exceeding (within observation statistics). Thus, we wish to solve the equation

$$\sum_{n=0}^{n_0} \sum_{i=0}^{n} \left(\frac{(\lambda_s)^i}{i!} e^{-\lambda_s}\right)\left(\frac{(\lambda_{b.g.})^{n-i}}{(n-i)!} e^{-\lambda_{b.g.}}\right) = 0.05 \tag{5.3}$$

for λ_s, where n_0 is the number of tracks observed in the region under consideration, λ_s is the expected number of source events, and $\lambda_{b.g.}$ is the expected number of background events. For the two cases under consideration, Equation 5.3 gives

$$\lambda_s e^{-\lambda_s}\left[\frac{(1.09)^0}{0!}\, e^{-1.09}\right] + 2e^{-\lambda_s}\left[\frac{(1.09)^1}{1!}\, e^{-1.09}\right]$$

$$= 0.336\,\lambda_s e^{-\lambda_s} + 0.732\, e^{-\lambda_s} = 0.05 \quad 30 \le E_\gamma \le 100 \text{ Mev}$$

and

$$e^{-\lambda_s}\left[\frac{(.14)^0}{0!}\, e^{-0.14}\right] = 0.05 \quad E_\gamma > 100 \text{ Mev}\,.$$

Solving these equations for λ_s, we obtain

$$\lambda_s = 3.6 \qquad 30 \le E_\gamma \le 100 \text{ Mev}$$

$$\lambda_s = 2.9 \qquad E_\gamma > 100 \text{ Mev}\,.$$

Finally, the 95-percent confidence flux upper limits are given by

$$F_{0.95}\,(30 \le E_\gamma \le 100) = \frac{3.6}{(7.05 \times 10^4 \text{ cm}^2 \text{ sec})\,\overline{(0.22)}}$$

$$= 2.3 \times 10^{-4} \text{ cm}^{-2} \text{ sec}^{-1} \tag{5.4a}$$

and

$$F_{0.95}\,(E_\gamma > 100) = \frac{2.9}{(7.3 \times 10^4 \text{ cm}^2 \text{ sec})\,\overline{(0.22)}}$$

$$= 1.8 \times 10^{-4} \text{ cm}^{-2} \text{ sec}^{-1}\,. \tag{5.4b}$$

3. Atmospheric Secondary Gamma-Ray Energy Spectrum

The data for the atmospheric spectrum, as previously mentioned, are taken from a balloon flight on December 10, 1966, from southern Australia. The data to be presented were obtained from a 2.1×10^4 second portion of the flight during which the balloon floated at 3 grams cm^{-2}. The average latitude was 33.7°S and the average longitude 139.0°E. The Quenby and Wenk (1962) vertical threshold rigidity for this location is 4.0 GV.

Of the 284 events selected as possible gamma-rays, we chose 222 whose opening angle was sufficiently large to discriminate between the electrons, for scattering by means of the scattering technique described in Chapter IV, Section 3. The third and first differences gave $(E_e)_{31}$ for each electron of the pair, and the added results gave the gamma-ray energy. For comparison, the energy for each gamma-ray was estimated on the basis of opening angle (as discussed in Chapter IV, Section 2). This energy estimate is crude, but the general agreement between the two methods is reassuring. Of the remaining 64 events in which the electron and position could not be resolved, 25 were judged to be Compton-scattered electrons, because electron-pairs with sufficient energy to show no separation should show no visible scattering. It will be seen that 25 is not an unreasonable number of Compton scattered electrons on the basis of the observed flux and the relative importance of the pair-production and Compton-scattering processes (see Figure 3.1).

Table 5.3 gives the observed number of gamma-rays in the various energy intervals. In view of the large uncertainties in the energy determination by the opening angle, the agreement between the two energy measurements is excellent in all but two energy intervals. The tendency to greatly underestimate the energy in a few cases, when using opening angle method, is probably due at least partly to the occasional sharp scatter, which tends to be somewhat smoothed out by the multiple-scattering technique. In the determination of the energy spectra, the scattering data will be used. To calculate the differential and integral intensities, we use the following equations:

$$I(E_1 \leq E_\gamma < E_2) = \frac{N(E_1 \leq E_\gamma < E_2)}{(E_2 - E_1) \cdot \alpha(E_\gamma) \cdot (A\Omega) \cdot t \cdot f} \tag{5.5a}$$

$$I(E_\gamma > E) = \left[\frac{N(E_\gamma > 250\ \text{Mev})}{\alpha E_\gamma} + \sum_{E_\gamma}^{2.50\ \text{Mev}} \frac{N(E_1 \leq E_\gamma < E_2)}{\alpha(E_\gamma)}\right] \frac{1}{(A \cdot \Omega) \cdot t \cdot f} \tag{5.5b}$$

Table 5.3

Energy Distribution of Observed Gamma-Rays.

Energy Interval (Mev)	Number of Gamma-Rays Observed	
	Scattering	Opening Angle
30 - 50	33	48
50 - 70	39	37
70 - 90	29	36
90 - 110	31	32
110 - 130	21	18
130 - 170	23	27
170 - 210	14	7
210 - 250	8	1
250	41	41
Unresolved pairs	66	66

where $N(E_\gamma > E)$ and $N(E_1 \leq E_\gamma < E_2)$ are the number of observed pairs in the energy ranges specified. The summation is taken over the discrete energy intervals listed in Table 5.3. t for the December 10, 1966, balloon flight is 2.1×10^4 seconds; f averaged over this duration is 0.48; and $\alpha(A\Omega)$ is taken from Figure 4.9.

The integral spectrum is plotted in Figure 5.2. The slope of -0.9 ± 0.1 at high energies and -0.5 ± 0.1 at low energies are in good agreement with the -0.87 ± 0.14 and -0.50 ± 0.06 observed by Frye *et al.* (1966), although the slope appears to break at a lower energy in this case. The high-energy slope is also in reasonable agreement with the measurements of Fazio *et al.* (1968) above about 300 Mev, though the latter spectrum appears to be flatter in the 100-300 Mev range than observed by most other investigators. The slope at lower energies also agrees with the measurements of Klarmann (1962) above 30 Mev.

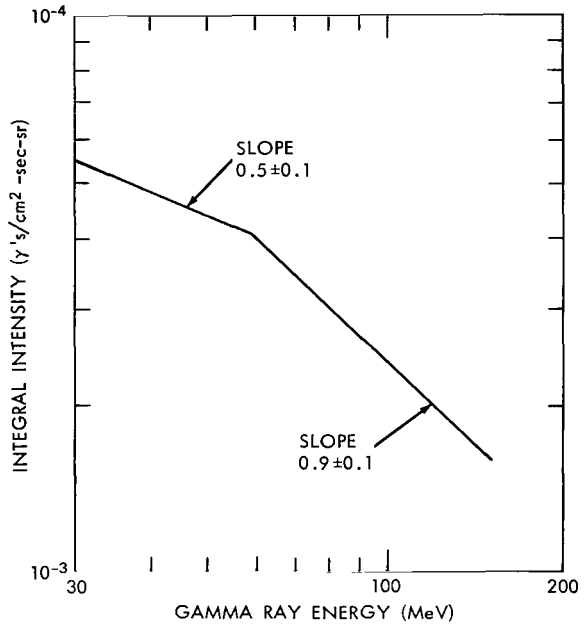

Figure 5.2—Observed integral intensity of atmospheric gamma-rays at an atmospheric depth of 3 g cm^{-2} and latitude 33.7° South.

Of the unresolved pairs listed in Table 5.3, 25 were classified as "single scatters." As stated in the last section, these tracks seem to be due to Compton scattered electrons. From the relative interaction coefficients of Figure 3.1, the observed number of pairs in Table 5.3, and the flat differential photon spectrum observed by Klarmann down to 5 Mev, we should expect 18 such Compton event. The difference between this and the observed number is insignificant, and probably results from cases where one electron of the pair receives insufficient energy and is absorbed before producing a spark.

CHAPTER VI

CONCLUSION

The limits of 2.3×10^{-4} cm^{-2} sec^{-1} ($30 \leq E_\gamma \leq 100$ Mev) and 1.8×10^{-4} cm^{-2} sec^{-1} ($E_\gamma > 100$ Mev) reported here are consistent with the theoretical predictions in Table 2.2 except for the extrapolated X-ray spectrum, which is expected to be an optimistic prediction as discussed in Chapter II. Proper operation of the detector for a full flight would approximately double this limit, with no additional improvements in the detector. Future flights will be made, using the same detector in a two-axis orientation gondola that keeps the detector pointing axis pointing at the source, thereby making the sensitivity equal to five times the previous figure. Additional improvements to increase the live time will again double the sensitivity.

The limits quoted represent improvements over all previously quoted results except the recent measurements quoted by Fazio *et al.* (1968), of 3.1×10^{-5} cm^{-2} sec for $E_\gamma > 100$ Mev, and earlier results by Cobb, *et al.* (1965), of 7×10^{-5} cm^{-2} sec^{-1}, and are in essential agreement with the results of Frye and Smith (1966), who quote a limit of 1.9×10^{-4} cm^{-2} sec^{-1} for the interval $30 \leq E_\gamma \leq 500$ Mev. The results of Fazio, *et al.*, and Cobb, *et al.*, are somewhat uncertain because both experiments observe an excessive number of "singles" tracks, and the results are sensitive to the method in which these tracks are treated, since an unknown fraction of them must be due to unresolved pairs. However, the uncertainty as to their methods is unlikely to affect their limits, except that Fazio, *et al.* seem to have summarily discarded such events with no appropriate correction. In that case, there would be an uncertainty of the order of a factor of two.

With these combined results, it appears quite safe to say that the limit on gamma-rays with energies greater than 30 Mev from the Crab nebula is of the order of 10^{-4} cm^{-2} sec^{-1}, and perhaps slightly lower. The best limit obtainable from balloons, as discussed in Chapter II, is probably about 10^{-5} cm^{-2} sec^{-1}, and the improved version of this experiment described above should be very close to this limit. From the theoretical predictions it can be seen that this sensitivity is unlikely to provide a detection of a gamma-ray point source in the Crab nebula or, probably, any other source, since similar theoretical calculations on other sources give similar or lower estimates. Thus, the best hope of detecting a point source of gamma-rays is a satellite experiment where the background contribution is significantly reduced, and the observed times correspondingly increased. The digitized spark chamber offers unique advantages over other types of detectors for a long-term satellite experiment, as detailed in Chapter III. A proposal by Cline, Fichtel, and Kniffen (1967) to place an enlarged version of the detector used in this experiment on an Explorer satellite indicates in detail the capability of obtaining limits of the order of 10^{-7} cm^{-2} sec^{-1} on any given source and of 10^{-6} cm^{-2} sec^{-1} on all sources in an all-sky survey. This experiment, to be flown on the SAS-B (Small Astronomy Satellite) Explorer, will provide detailed information

on the energy and spatial distribution of the diffuse intensity of gamma-rays recently observed by Clark, *et al.* (1968) on OSO-3. This information is needed to aid in the understanding of the unexpectedly high measured intensities.

In summary, the chance of detecting point sources of gamma-rays from balloons seems remote, though a thorough search over the entire sky with sensitivities down to about 10^{-5} cm^{-2} sec^{-1} is possible and should be made. The best chance is to make a long-term satellite exposure that allows a measurement of the isotropic intensity not possible in balloon experiments. The digitized spark chamber has many features that make it perhaps the best available gamma-ray detector for such a satellite experiment.

The method of measuring energy described in Chapter IV, based on multiple Coulomb scattering, represents an important technical advance. Its ability to obtain gamma-ray energy spectra, without the added weight and volume of special active devices, make it ideal for use in space. Within the limits of the uncertainty, the spectra so obtained agree with previously reported data; further refinement and calibration should improve the results.

Acknowledgments

A deep debt of gratitude is due to Dr. Carl E. Fichtel, who suggested the topic and contributed numerous invaluable suggestions and discussions during the course of the work. For engineering and technical support during all phases of the detector development and in the field I am grateful to Messrs. R. W. Ross, C. H. Ehrmann, J. W. O'Connor, W. J. Hungerford, A. F. Mascaro, R. L. Smith, Jr., S. M. Derdeyn, E. Martinez, A. M. Marshall, V. P. Cogan, J. G. Etzel, and L. J. Horning. For their assistance in the data reduction I should like to thank Mrs. H. H. Marsh, Mr. E. R. Whitehurst, and Mr. D. S. Elliot. For balloon flight support I am indebted to Mr. H. Dembowski and Cdr. D. Sumner of the Office of Naval Research, who arranged the balloon flights; to Mr. T. J. Danaher, Lt. Col. R. C. Clemenson, and the balloon launch team of the Air Force Cambridge Research Laboratory, who provided the launch services for the New Mexico flight; and to Mr. W. Marlowe of the AEC, Dr. E. J. Herbert, Mr. E. Curwood, and the balloon launch team of the Australian Department of Supply, who provided the launch services for the Australian flight.

Goddard Space Flight Center
National Aeronautics and Space Administration
Greenbelt, Maryland, February 9, 1968
879-10-01-01-51

REFERENCES

"American Ephemeris and Nautical Alamanac for the Year 1967," Washington, U. S. Government Printing Office, 1965.

Annis, M., Bridge, H. S., and Olbert, S., "Application of the Multiple Scattering Theory to Cloud-Chamber Measurements II," *Phys. Rev.* 89:1216-1227, 1953.

Bethe, H., "Moliere's Theory of Multiple Scattering," *Phys. Rev.* 89:1256-1266, 1953.

Bowyer, S., Byram, E. T., Chubb, T. A., and Friedman, H., "X-ray Sources in the Galaxy," *Nature* 201:1307-1308, 1964.

Bracessi, A., and Ceccarelli, M., and Salander, S., "Search for γ-Radiation from the Cygnus A Radio Source," *Il Nuovo Cimento* 17:691-694, 1960.

Clark, G. W., "Balloon Observations of the X-Ray Spectrum of the Crab Nebula above 15 KeV," *Phys. Rev. Letters* 14:91-94, 1965.

Clark, G. W., Garmire, G. P., and Kraushaar, W. L., "Observation of High-Energy Cosmic Gamma Rays," *Ap. J. Letters*, 153:L203-L207, 1968.

Cline, T. L., "Search for High-Energy Cosmic Gamma Rays," *Phys. Rev. Letters* 7:109-112, 1961.

Cline, T. L., Fichtel, C. E., and Kniffen, D. A., "Proposal to Pursue High-Energy Gamma-Ray Astronomy Using a Digitized Spark Chamber on an Explorer," NASA Goddard Space Flight Center Document X-611-67-135, 1967.

Cobb, R., Duthie, J. G., and Stewart, J., "Spark-Chamber Experiment on Cosmic Gamma Rays," *Phys. Rev. Letters* 14:507-511, 1965.

Danielson, R. E., "An Attempt to Detect Energetic Gamma Radiation from the Sun," *J. Geophys. Rad.* 65:2055-2059, 1960.

Delvaille, J. P., Albats, P., Greisen, K. I., and Ögelman, H. B., "Search for Point Source of High Energy Cosmic Gamma Rays," *Can. J. Phys.* 46:S425-S426, 1968.

Dolan, J. F., and Fazio, G. G., "The Gamma-Ray Spectrum of the Sun," *Rev. Geophys.* 3:319-393, 1965.

Druyvesten, M. J., and Penning, F. M., "The Mechanism of Electrical Discharges in Gases of Low Pressure," *Rev. Mod. Phys.* 12:87-174, 1940.

Duthie, J. G., Cobb, R., and Stewart, J., "Evidence for a Source of Primary Gamma Rays, *Phys. Rev. Letters* 17:263-267, 1966.

Earl, J. A., "Cloud-Chamber Observations of Primary Cosmic-Ray Electrons," *Phys. Rev. Letters* 6:125-128, 1961.

Fazio, G. G., "Gamma Radiation From Celestial Objects," in "Annual Rev. Astron. and Astrophys.," 5 (ed. L. Golberg, Palo Alto: Annual Rev. Inc., 1967), 481-524, 1967.

Fazio, G. G., and Hafner, E. M., "The OSO1 High-Energy Gamma-Ray Experiment," *J. Geophys. Res.* 72:2452-2455, 1967.

Fazio, G. G., and Helmken, H. F., "Application of the Vidicon Spark-Chamber to Gamma-Ray Astronomy from High-Altitude Balloons and Satellites," *Can. J. Phys.* 46:S456-S460, 1968.

Fazio, G. G., Helmken, H. F., Cavrak, S. J., and Hearn, D. R., "Search for Cosmic Gamma Radiation with a Vidicon Spark Chamber," *Can. J. Phys.* 46:S427-S432, 1968.

Feenberg, E., and Primakoff, H., "Interaction of Cosmic-Ray Primaries with Sunlight and Starlight," *Phys. Rev.* 73:449-469, 1948.

Felten, J. E., and Morrison, P., "Recoil Photons from Scattering of Starlight by Relativistic Electrons," *Phys. Rev. Letters* 10:453-457, 1963.

Fermi, E., "Nuclear Physics," notes compiled by J. Orear, A. H. Rosenfeld, and R. A. Schluter, Chicago: Univ. of Chicago Press, 1955.

Fichtel, C. E., Cline, T. L., Ehrmann, C. H., Kniffen, D. A. and Ross, R. W., "Gamma-ray Astronomy with a Digitized Spark Chamber," *Can. J. Phys.*, 46:S419-S424, 1968.

Fichtel, C. E., and Kniffen, D. A., "A Search for Gamma-Ray Point Sources," *J. Geophys. Res.* 70(17):4227-4234, 1965.

Fischer, J., and Zorn, G. T., "Observations on Pulsed Spark Chambers," *Reviews of Scientific Instruments* 32:499-508, 1961.

Fowler, P. H., "XV, "Nuclear Transmutations Produced by Cosmic-Ray Particles of Great Energy III," *Phil. Mag.* XLI:169-184, 1950.

Frost, K. J., Rothe, E. D., and Peterson, L. E., "A Search for the Quiet-Time Solar Gamma-Rays from Balloon Altitudes," *J. Geophys. Res.* 71:4079-4089, 1966.

Frye, G. M., Jr., Reines, F., and Armstrong, A. H., "Search for Solar and Cosmic Gamma-Rays," *J. Geophys. Res.* 71:3119-3123, 1966.

Frye, G. M., Jr., and Smith, L. H., "Upper Limits to Cosmic Rays in the Range 30 to 500 MeV," *Phys. Rev. Letters* 17:733-736, 1966.

Frye, G. M., Jr., and Wang, C. P., "On the Reported Cosmic Ray Source in Cygnus," *Phys. Rev. Letters* 18:132-134, 1967.

Frye, G. M., Jr., and Wang, C. P., "Search for Gamma Rays from 3C273 and M87," *Can. J. Phys.* 46:S448-S450, 1968.

Garmire, G., and Kraushaar, W. L., "High Energy Cosmic Gamma Rays," *Space Sci. Rev.* 4:123-146, 1965.

Ginzburg, V. L., and Syrovatskii, S. J., "Origin of Cosmic Rays," translated by H. S. H. Massey, ed. D. ter Haar. New York: Macmillan Co., 1964.

Ginzburg, V. L., and Syrovatskii, S. J., "Some Problems of Gamma- and X-Ray Astronomy," *Soviet Phys. - Uspekhi* 7:696-720, 1965.

Goudsmit, S., and Saunderson, J. L., "Multiple Scattering of Electrons," *Phys. Rev.* 57:24-29, 1940.

Gould, R. J., and Burbidge, G. R., "High Energy Cosmic Photons and Neutrinos," *Annales d'Astrophys.* 28:171-201, 1965.

Greisen, K., "Experimental Gamma-Ray Astronomy," in "Perspectives in Modern Physics," ed. R. E. Marshak, New York: Interscience, 1966, pp. 355-382.

Hayakawa, S., Okuda, H., Tanaka, Y., and Yammamoto, Y., "Cosmic Electrons and Gamma-Rays," Supplement of the Progress in Theoretical Physics, 30:153-203, 1964.

Heitler, W., "The Quantum Theory of Radiation," 3rd edition, London: Oxford Univ. Press, 1954.

Hess, W. N., and Mead, G. D. (ed.), "Introduction to Space Sciences," 2nd ed., New York: Gordon and Breach, 1967.

Klarmann, J., "A Search for High-Energy Cosmic γ-Rays in Emulsions," *Il Nuovo Cimento* 24: 540-545, 1962.

Kraushaar, W. L., and Clark, G. W., "Some Experimental Attempts to Detect Cosmic Gamma Rays," *J. Phys. Soc. of Japan* Supplement A-III 1-5, 1962a.

Kraushaar, W. L., and Clark, G. W., "Search for Primary Cosmic Gamma Rays with the Satellite Explorer XI," *Phys. Rev. Letters* 8:106-109, 1962b.

Kraushaar, W. L., Clark, G. W., Garmire, G., Helmken, H., Higbie, P., and Agogino, M., "Explorer XI Experiment on Cosmic Gamma Rays," *Astrophys. J.* 141:845-863, 1965.

Meek, J. M., and Craggs, J. D., "Electrical Breakdown of Gases," London: Oxford Univ. Press, 1953.

Moliere, G., "Theorie der Streuung Schneller Geladener Teilchen I," *Zeit. für Naturforschung* 2a: 133-145, 1947.

Moliere, G., "Theorie der Streuung Schneller Geladener Teilchen II," *ibid.* 3a:78-97, 1948.

Moliere, G., "Theorie der Streuung Schneller Geladener Teilchen III," *ibid.* 10a:177-211, 1955.

Morrison, P., "On Gamma-Ray Astronomy," *Il Nuovo Cimento* 7:858-864, 1958.

Oda, M., "X-ray and γ-ray Astronomy," Proceedings of the Ninth International Conference on Cosmic Rays, London, 1965, pp. 65-80.

Olbert, S., "Application of the Multiple Scattering Theory to Cloud-Chamber Measurements. I," *Phys. Rev.* 87:319-327, 1952.

Olsen, H., "Opening Angles of Electron-Positron Pairs," *Phys. Rev.* 131:406-415, 1963.

Perlow, G. J., and Kissinger, C. W., "A Search for Primary Gamma-Radiation. I," *Phys. Rev.* 81:552-554, 1951.

Peterson, L. E., Jacobson, A., and Pelling, R. M., "Spectrum of Crab Nebula X-Rays to 120 KeV," *Phys. Rev. Letters* 16:142-144, 1966.

Pinkau, K., "Moliere's Theory of Multiple Scattering Applied to the Spark Chamber," *Zeit. Phys.* 196:163-173, 1966.

Pinkau, K., "The Measurement of Multiple Scattering of Track Direction and Position in Spark Chambers," *Nuclear Instruments and Methods* 48:173-174, 1967.

Pollack, J. B., and Fazio, G. G., "Production of Mesons and Gamma Radiation in the Galaxy by Cosmic Rays," *Phys. Rev.* CXXXI:2684, 1963.

Quenby, J. J., and Wenk, G. J., "Cosmic Ray Threshold Rigidities and the Earth's Magnetic Field," *Phil. Mag.* 7:1457-1485, 1962.

Raether, H., "Electron Avalanches and Breakdown in Gases," Washington: Butterworth & Co., 1964.

Rossi, B., "High-Energy Particles," Englewood Cliffs, N. J.: Prentice-Hall, Inc., 1952, pp. 77-86.

Rossi, B., "Experimental X-Ray Astronomy," in "Perspectives in Modern Physics," ed. R. E. Marshak, New York: Interscience, 1966.

Savedoff, M. D., "The Crab and Cygnus A as Gamma Ray Sources," *Il Nuovo Cimento* 13:12-18, 1959.

Sartori, L., and Morrison, P., "Thermal X-Rays from Non-Thermal Radio Sources," *Astrophys. J.* 150 (2, Part 1):385-403, 1967.

Schneider, F., "The Multiple Track Efficiency of the Spark Chamber," (CERN Internal Report, 1963), AR/Int. GS/63-9.

Scott, W. T., "Mean-Value Calculations for Projected Multiple Scattering," *Phys. Rev.* 85:245-248, 1952.

Shklovskii, I. S., "Cosmic Radio Waves," translated by R. B. Rodman and C. M. Varsavsky, Cambridge: Harvard Univ. Press, 1960.

Snyder, H., and Scott, W. T., "Multiple Scattering of Fast Charged Particles," *Phys. Rev.* 76:220-225, 1949.

Svensson, G., "The Cosmic Ray Photon and μ-meson Energy Spectra at 29-30 km above Sea Level," *Azkiv ta Fysik* 13:347, 1958.

Voyvodic, L., and Pickup, E., "Multiple Scattering of Fast Particles in Photographic Emulsions," *Phys. Rev.* 85:91-100, 1952.

Williams, E. J., "Concerning the Scattering of Fast Electrons and of Cosmic Ray Particles," *Proc. Roy. Soc. London* 169:531-572, 1939.

Appendix A

Calculation of Geometric Factor

The geometry of the cone acceptance of the spark chamber is defined by the 6-inch-square acceptance area at the top of the detector and the circular Čerenkov detector at the bottom.

For any two plane, parallel, axially symmetric area elements, separated by a distance d, the elemental geometric factor is given by

$$dG(d) = \frac{(d\vec{A}_1 \cdot \vec{\ell})(d\vec{A}_2 \cdot \vec{\ell})}{\ell^4}$$

where A_1 and A_2 are the areas of the top and bottom area elements of the acceptance cone, respectively, and $d = d\vec{A} \cdot \vec{\ell}/|dA|$ for the case where $d\vec{A}_1$ and $d\vec{A}_2$ are parallel. In Figure A1 it can be seen that ℓ can be defined by $\ell^2 = d^2 + q^2 + r^2 - 2qr\cos(\phi_2 - \phi_1)$. Thus the total geometric factor is given by

$$G(d) = 8d^2 \int_0^{\pi/4} d\phi_1 \int_0^{x/\cos\phi_1} (dq)\, q \int_0^{R} (dr)\, r \int_0^{2\pi} \cdot d\phi_2 \left[d^2 + q^2 + r^2 - 2qr\cos(\phi_2 - \phi_1)\right]^{-2}, \quad \text{(A1)}$$

where $L = 2x$ is the linear dimension of one side of the upper square element and R the radius of the lower circular element. Equation A1 cannot be integrated in closed form; however, expanding the integrand in powers of d^{-2} (assuming $L^2 + 4R^2 < 2d^2$), keeping the first three terms, and performing the indicated integration term by

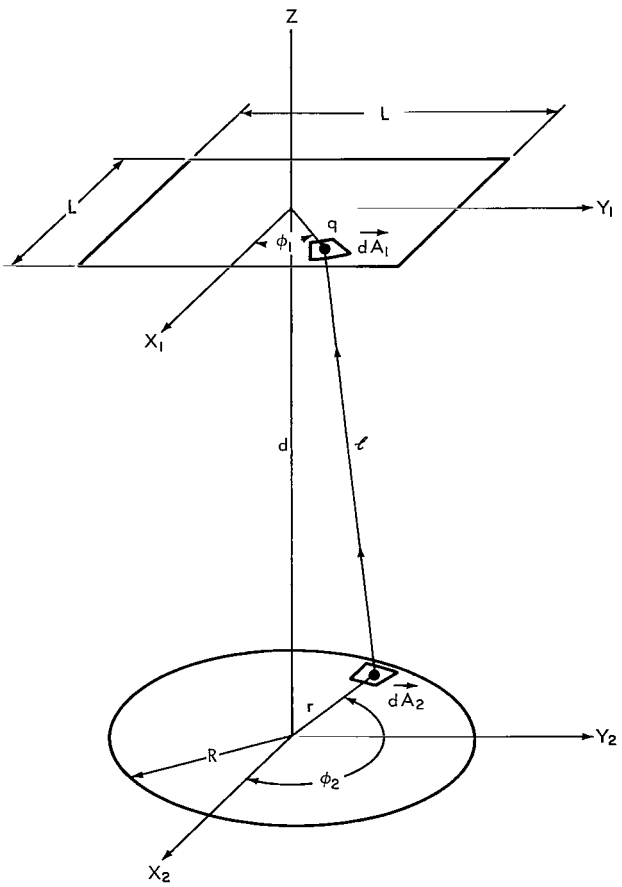

Figure A1—Coordinate system for calculating the geometric factor for asymptotically high gamma-ray energies.

term gives:

$$G(d) = \frac{16\pi R^2 x^2}{d^2}\left[\frac{1}{4} - \frac{1}{d^2}\left(\frac{x^2}{3} + \frac{R^2}{4}\right) + \frac{1}{d^4}\left(\frac{R^4}{4} + R^2 x^2 + \frac{7}{15} x^4\right) + \cdots\right]$$

$$= \frac{A_1 A_2}{d^2}\left[1 - \frac{1}{d^2}\left(\frac{A_1}{3} + \frac{A_2}{\pi}\right) + \frac{1}{d^4}\left(\frac{A_2^2}{\pi^2} + \frac{A_2 A_1}{\pi} + \frac{7}{60} A_1^2\right) + \cdots\right]. \qquad \text{(A2)}$$

For the spark chamber used in this experiment, $A_1 = 232$ cm^2, $A_2 = 100$ cm^2, and $d = 30.6$ cm. Therefore $G(d) = 24.8$ cm^2 steradian. The geometric factor, based solely on the detector geometry, represents the asymptotic geometric factor at high gamma-ray energies. As the energy decreases, scattering of the electrons becomes a significant factor, as discussed in Section 5 of Chapter IV.

Appendix B

List of Symbols

$a = \ell/2$ = half the distance between spark electrodes

a_f = Fermi radius of the atom

c = speed of light

d = thickness of scattering plates

e = electronic charge

f = percentage detector "live" time

ℓ = distance between spark electrodes

m = mass of atoms

m_e = mass of the electron

n = density of atoms

n_c = number of ferrite cores set in one event

n_e = electron number density

n_0 = scattering deflection due to random-noise signal

$\bar{n}_0$ = noise scattering signal

n_p = number of scattering plates through which electrons have passed between measurements

$\bar{n}_{ph}$ = average photon number density

p = pressure expressed in atmospheres

$p(\nu, E_e)$ = power radiated by an electron of energy E_e

$q_e(E_e)$ = differential electron source production spectrum

$q_\gamma(E_\gamma)$ = differential photon source production spectrum

r_e = classical radius of the electron

r_L = Larmor radius

s = distance from the earth to the photon source

t = time

v_e = velocity of electron

V_0 = volume of the region of photon emission

V_p = potential applied across the spark electrodes

x_c = critical distance for streamer formation

A = sensitive area of the detector

A_s = atomic weight of scattering material

C = proportionality constant of observed spectral flux

E_e = kinetic energy of the electron

E_r = spherical space-charge field

E_r' = energy of electron subsequent to Compton scattering in the rest frame of the primary electron

$F(\nu)$ = frequency-dependent photon flux

$F_{\gamma,br}(E_\gamma)$ = flux emission, expected to be observed at the earth, of photons of energy E_γ due to bremsstrahlung emission by electrons traveling within the material of the source

$F_{\gamma,comp}(E_\gamma)$ = flux emission, expected to be observed at the earth, of photons of energy E_γ due to Compton scattering of low-energy photons by energetic electrons

$F_{\gamma,min}$ = minimum point-source gamma-ray flux that can be detected at the earth

$F_{\gamma,\pi 0}(E_\gamma)$ = flux emission, expected to be observed at the earth, of photons due to the decay of neutral pions produced in nuclear collisions

$F_{\gamma,sync}(\nu)$ = frequency-dependent flux of photons, expected to be observed at the earth, due to synchrotron emission by electrons in the source

H = magnetic field strength

$H_\perp$ = component of magnetic field perpendicular to plane of particle orbit

$I_{\gamma,b.g.}$ = diffuse background gamma-ray intensity

K_e = proportionality constant of power-law electron-number spectrum

K_π = proportionality constant of power-law pion-number spectrum

M = total mass with source = $\int_{\text{source}} m \, dV_0$

N = number of secondary electrons required to produce a streamer

N_s = density of atoms in the scattering material

N_γ = number of observed gamma-rays

N_σ = signal-to-noise ratio

N_0 = number of primary electrons produced per centimeter at a pressure of one atmosphere due to ionization

P_r' = the longitudinal momentum of the electron subsequent to Compton scattering in the rest frame of the primary electron

X = radiation length

X_0 = radiation length of scattering material

Z_s = atomic number of scattering material

α = detector efficiency for gamma-ray detection

α_ν = spectral index of observed photon frequency spectrum

$\alpha_s = Z_s/137$ (for relativistic electrons)

α_T = Townsend's first ionization coefficient

$\beta_e = v_e/c$

β_{n_p} = scattering signal for electron passing through n_p plates

β_s = Coulomb scattering signal

$\gamma = 1/\sqrt{1-\beta_e^2}$

ϵ_ℓ = energy of photon in frame of observation before scattering

ϵ_ℓ' = energy of photon in frame of observation after scattering

ϵ_r = energy of photon in rest frame before Compton scattering

ϵ_r' = energy of photon in rest frame after Compton scattering

η = spark efficiency for one spark gap

θ = complement of angle between direction of velocity vector primary electron and photon before scattering

θ = measured opening angle of electron-positron pair

θ' = complement of angle between direction of velocity vector primary electron and photon after scattering

λ = de Broglie wavelength of the electron

ν = photon frequency

ρ_{ph} = energy density of photon field

ρ_s = density of scattering material

$\sigma_{rad}(E_e, E_\gamma)$ = the differential cross section for the emission of a photon of energy E_γ by an electron of energy E_e

σ_T = the total Thomson cross section

τ = characteristic time for pion production in the source region

τ_d = spark-discharge time constant

τ_{sync} = characteristic time for synchrotron emission due to bremsstrahlung radiation

$\Delta = 2a + d$

Γ_e = exponent of negative power-law electron-number density spectrum

Γ_π = exponent of negative power-law pion-number density spectrum

χ_r = angle between photon velocity vector before and after Compton scattering

Ω = solid angle

"The aeronautical and space activities of the United States shall be conducted so as to contribute . . . to the expansion of human knowledge of phenomena in the atmosphere and space. The Administration shall provide for the widest practicable and appropriate dissemination of information concerning its activities and the results thereof."

—NATIONAL AERONAUTICS AND SPACE ACT OF 1958

NASA SCIENTIFIC AND TECHNICAL PUBLICATIONS

TECHNICAL REPORTS: Scientific and technical information considered important, complete, and a lasting contribution to existing knowledge.

TECHNICAL NOTES: Information less broad in scope but nevertheless of importance as a contribution to existing knowledge.

TECHNICAL MEMORANDUMS: Information receiving limited distribution because of preliminary data, security classification, or other reasons.

CONTRACTOR REPORTS: Scientific and technical information generated under a NASA contract or grant and considered an important contribution to existing knowledge.

TECHNICAL TRANSLATIONS: Information published in a foreign language considered to merit NASA distribution in English.

SPECIAL PUBLICATIONS: Information derived from or of value to NASA activities. Publications include conference proceedings, monographs, data compilations, handbooks, sourcebooks, and special bibliographies.

TECHNOLOGY UTILIZATION PUBLICATIONS: Information on technology used by NASA that may be of particular interest in commercial and other non-aerospace applications. Publications include Tech Briefs, Technology Utilization Reports and Notes, and Technology Surveys.

Details on the availability of these publications may be obtained from:

SCIENTIFIC AND TECHNICAL INFORMATION DIVISION

NATIONAL AERONAUTICS AND SPACE ADMINISTRATION

Washington, D.C. 20546